Contents

List of Figures

List of Tables

Chapter 1

Structure and equation of state of cold non-accreting neutron stars

This chapter deals with the structure and equation of state (EoS) of neutron stars (NS) within the framework of the "cold catalyzed matter" (CCM) hypothesis.

With typical temperature of about $T \sim 10^8$ K ~ 0.01 MeV$/k_B$, NS are very cold systems from the nuclear physics viewpoint, therefore the CCM hypothesis is commonly used to predict their internal composition and pressure. In this limit, thermal, nuclear, and beta equilibrium are established at zero temperature, meaning that the energy cannot be lowered by weak, strong, or electromagnetic processes, thus the matter is in its ground state. It is reasonable to expect these equilibrium conditions to be valid in any NS as far as it is not accreting matter from a neighbor. Indeed, in the accretion scenario, the typical timescale of the process are such that the matter composition is believed to be out of equilibrium.

As already discussed in the general introduction, the EoS relates, in given conditions of temperature and densities, the macroscopic quantities of the star, such as the mass density and the pressure, which determines among others the mass-radius relation of NS. The evaluation of the EoS therefore implies to know the microscopic composition at each point in the star. At subsaturation densities, the solid crust consists mainly of clusterized matter, arranged in a body-centered cubic lattice [HPY07]. The relevant degrees of freedom in the crust are the Wigner-Seitz (WS) cells, containing exactly one lattice point [WS33]. At zero temperature, WS cells are supposed to be identical, thus the so-called single nucleus approximation (SNA), which considers a unique configuration for a given thermodynamic condition of temperature and pressure (P, T), becomes exact. The ground state of the outer crust is almost entirely characterized by experimental nuclear masses, which are available up to $(N - Z)/A \lesssim 0.3$. The determination of inner-crust ground state is however more challenging because the crust is permeated by free neutrons, a situation which cannot be achieved in terrestrial conditions. Therefore, different treatments, from microscopic [NV73] to classical [BBP71], can be envisaged to estimate the energy of matter, and the EoS in this region depends on the nucleon-nucleon (NN) effective interaction or energy functional. At suprasaturation densities, matter consists of a uniform plasma of neutrons, protons, electrons, and eventually muons, in both strong and weak equilibrium. The development of a unified EoS, that is such that

matter at subsaturation and supersaturation densities are treated within a unique model, is essential if one wants to make realistic predictions on NS observables [For+16].

The plan of the chapter is as follows. In Section 1.1, the ground state of the outer crust is determined by application of the method introduced by Baym, Pethick, and Sutherland (BPS) [BPS71], using experimental masses [Hua+17] supplemented by state-of-the-art microscopic theoretical mass tables. Section 1.2 is devoted to the determination of the inner-crust ground state using a compressible liquid drop model (CLDM) based on the metamodeling technique [MHG18a; CGM19]. The phase transition from the solid crust to the liquid core, occuring at some ≈ 1 km from the surface of the star, is investigated. In Section 1.3, we calculate the ground state of matter in the outer core, and we address the problem of the inner-core composition. In Section 1.4, a unified metamodeling of the EoS is proposed. Finally, conclusions are given in Section 1.5.

1.1 Ground state of the outer crust

At zero temperature, the matter inside the outer crust corresponds to a lattice of strongly bound nuclei, immersed in an sea of electrons. The mass density at which nuclei are fully ionized and electron completely degenerated is of the order of $\rho \gg 6AZ \sim 10^4$ g/cm^3 for ^{56}Fe, which is the ground state of matter at very low density. Below 10^4 g/cm^3, some electrons are still bound to the nuclei and one must rely on the EoS calculated by Feynman, Metropolis, and Teller from 15 to 10^4 g/cm^3, suitable for the envelope of neutron stars [FMT49].

This section deals with the determination of the outer-crust ground state. In 1.1.1, we detail the different terms entering in the WS cell energy, with emphasis on the relativistic electron gas energy as well as nuclear masses. The ground state of the outer crust is calculated by application of the variational BPS method [BPS71], which is presented in 1.1.2. Finally, using current knowledge on experimental masses [Hua+17] supplemented by different microscopic theoretical mass tables, we compute the equilibrium composition and EoS. Our results are presented in 1.1.3.

1.1.1 Wigner-Seitz cell energetics

In the outer crust, a WS cell is composed of a strongly bound nucleus at the center, immersed in a relativistic electron gas of density n_e. Charge neutrality is assured in each unit cell, $n_e = n_p$, with n_p the proton density inside the cell.

The energy of a WS cell in the outer crust can therefore be written as

$$E_{WS} = E_i + V_{WS}\varepsilon_e, \tag{1.1}$$

with E_i the ion energy, V_{WS} the volume of the cell, and ε_e the energy density of the relativistic electron gas. The ion energy reads

$$E_i = M'(A,Z)c^2 + E_L + E_{zp}, \tag{1.2}$$

where $M'(A,Z)c^2$ is the nuclear mass of a nucleus with associated mass number A and charge number Z, E_L the temperature-independent static-lattice term, and E_{zp} the

zero-point quantum vibration term given by

$$E_{zp} = \frac{3}{2}\hbar w_p u_1, \tag{1.3}$$

where $u_1 = 0.5113875$ is a numerical constant for a body-centered cubic lattice (see Table 2.4 of [HPY07]), which is assumed to be the geometry minimizing the lattice energy. This assumption was recently confirmed in [CF16]. The ion plasma frequency w_p is given by

$$\hbar w_p = \sqrt{\frac{(\hbar c)^2 4\pi n_N (Ze)^2}{M'(A,Z)c^2}}, \tag{1.4}$$

e being the elementary charge, c the speed of light, $\hbar = h/2\pi$ the reduced Planck constant, and where the ion density $n_N = 1/V_{WS}$ has been introduced.
The lattice energy reads

$$E_L = -C_M \frac{(Ze)^2}{a_N}, \tag{1.5}$$

with $C_M = 0.895929255682$ the Mandelung constant for a body-centered cubic lattice (see Table 2.4 of [HPY07]), and $a_N = (4\pi n_N/3)^{-1/3}$ the ion-sphere radius.

1.1.1.1 Nuclear mass tables

An essential input for Eq. (1.2) is the nuclear mass table. When available, that is for $I = (N-Z)/A \lesssim 0.3$, we use experimental masses from the 2016 Atomic Mass Evaluation (AME) [Hua+17]. For more neutron-rich nuclei and until we reach the neutron drip line, the use of a model is required, thus a model dependence arises. A possibility is to rely on microscopic Hartree-Fock-Bogoliubov (HFB) theoretical mass tables [Sam+02], which are based on the nuclear energy-density functional theory that is discussed in the general introduction.

In general, atomic masses are tabulated instead of the nuclear ones which can be calculated as

$$M'(A,Z)c^2 = M(A,Z)c^2 - Zm_e c^2 + B_e(Z), \tag{1.6}$$

with $M(A,Z)c^2 = \Delta\epsilon + Am_u c^2$ the atomic mass ($\Delta\epsilon$ is the mass excess, m_u is atomic mass unit), m_e the electron mass, and B_e the binding energy of atomic electrons depending solely on the number of protons Z according to the approximation proposed in [LPT03] (see their Eq. (A4)),

$$B_e(Z) = 1.44381 \times 10^{-5} Z^{2.39} + 1.55468 \times 10^{-12} Z^{5.35}. \tag{1.7}$$

1.1.1.2 Relativistic electron gas

In the outer crust, the mass densities are above $\sim 10^4$ g/cm^3 therefore the electrons are essentially free.
The expression of the energy density of a relativistic electron gas, with rest mass energy, at zero temperature can be calculated as

$$\begin{aligned} \varepsilon_e(n_e) &= \int_0^{k_e} \frac{k^2 dk}{\pi^2} c\sqrt{\hbar^2 k^2 + {m_e}^2 c^2} \\ &= \frac{P_r}{8\pi^2}\left[x_r(1+2{x_r}^2)\gamma_r - \ln(x_r+\gamma_r)\right], \end{aligned} \tag{1.8}$$

with $P_r = {m_e}^4 c^5/\hbar^3$ the relativistic unit of the electron pressure, $x_r = \hbar k_e/(m_e c)$ the relativity parameter, and $\gamma_r = \sqrt{1+{x_r}^2}$. k_e is the electron Fermi wave number given by

$$k_e = (3\pi^2 n_e)^{1/3}. \tag{1.9}$$

The derivation of Eq. (1.8) is given in Appendix A.
Above 10^7 g/cm^3, $x_r \gg 1$, thus electrons can be considered ultrarelativistic and Eq. (1.8) becomes

$$\varepsilon_e(n_e) = \frac{3}{4} n_e m_e c^2 x_r. \tag{1.10}$$

Taking the derivative of Eq. (1.8) with respect to the electron gas density yields the pressure,

$$\begin{aligned} P_e &= -\frac{\partial(V_{WS}\varepsilon_e)}{\partial V_{WS}} = n_e \frac{\partial \varepsilon_e}{\partial n_e} - \varepsilon_e \\ &= \frac{P_r}{8\pi^2}\left[x_r(1+2{x_r}^2)\gamma_r - \ln(x_r+\gamma_r)\right]. \end{aligned} \tag{1.11}$$

The exchanges and correlation corrections are neglected since they are known to be small in comparison to the kinetic energy of relativistic electrons. The expression of the exchange correction to the free energy density for a strongly degenerate electron gas is given in [HPY07] (see their Eq. (2.151)). We have checked that the inclusion of these corrections does not modify the results presented in this chapter.

1.1.2 The BPS model

The variational technique which is currently used to calculate the ground state of the outer crust was introduced by Baym, Pethick, and Sutherland in [BPS71].

The zero-temperature Gibbs free energy per nucleon is the quantity to be minimized at fixed pressure P under the condition of charge neutrality $n_e = Z n_N$, until the neutron drip sets in, the condition for which is $\mu_n = m_n c^2$, with μ_n the neutron chemical potential, and m_n the neutron mass.

The definition of the zero-temperature Gibbs free energy per nucleon is

$$g = \frac{\varepsilon_{WS} + P}{n_B}, \tag{1.12}$$

where $\varepsilon_{WS} = E_{WS}/V_{WS}$ is the energy density of the WS cell, and n_B is the baryon density given by $n_B = n_N A = A/V_{WS}$.
We can calculate the pressure as

$$P = {n_B}^2 \frac{\partial(\varepsilon_{WS}/n_B)}{\partial n_B}\Big|_{Z,A}, \tag{1.13}$$

yielding, using Eq. (1.1),

$$P = P_e + \frac{1}{3} E_L n_N + \frac{1}{2} E_{zp} n_N. \tag{1.14}$$

Thus the expression of the zero-temperature Gibbs free energy per nucleon can be rewritten as

$$g = \frac{M'(A,Z)c^2 + \frac{4}{3}E_L + \frac{1}{2}E_{zp} + Z\mu_e}{A}, \tag{1.15}$$

where μ_e is the electron chemical potential given by

$$\mu_e = \frac{\partial \varepsilon_e}{\partial n_e}. \tag{1.16}$$

Essentially, one fixes the pressure P, calculates for each nucleus (A, Z) the electronic density by solving numerically Eq. (1.14), then constructs a table (g, A, Z). The ground state of the outer crust at pressure P then corresponds to the nucleus associated to the minimum value of g.

As explained in [Pea+18], the neutron chemical potential can be calculated through

$$\mu_n = g, \tag{1.17}$$

because the beta equilibrium equation $\mu_n = \mu_p + \mu_e$ holds throughout the star. Indeed, by exploiting the thermodynamic relation

$$\mathcal{G} = \varepsilon + P = \mu_n n_n + \mu_p n_p + \mu_e n_e, \tag{1.18}$$

together with the charge neutrality condition $n_e = n_p$, we obtain

$$\mathcal{G} = \mu_n n_n + (\mu_e + \mu_p) n_p, \tag{1.19}$$

where $\mathcal{G}$ is the zero-temperature Gibbs free energy density, and μ_p the proton chemical potential. In the case where the chemical equilibrium is established, that is if weak processes are at the equilibrium, we finally get

$$\mathcal{G} = \mu_n n_B. \tag{1.20}$$

One should stress that while minimizing the zero-temperature Gibbs free energy per nucleon at fixed pressure is less practical than simply minimizing the total energy density at constant baryon density, it makes it easier to study the transitions between layers. The pressure increases continuously with increasing depth in the star, thus a discontinuity in the density is the signature of a transition from a layer (A, Z) to another (A', Z'). Noting that the pressure in the outer crust is approximately equal to the pressure of the electron gas (the lattice and zero-point terms contribute to less than 5% to the total pressure in the bottom layers of the outer crust), we know that $n_e = n_p$ is continuous across the transition thus

$$\Delta n_B = n'_B - n_B \simeq n_p \left(\frac{A'}{Z'} - \frac{A}{Z} \right), \tag{1.21}$$

and the fractional change in the baryon mass density results

$$\frac{\Delta \rho_B}{\rho_B} \simeq \frac{\Delta n_B}{n_B} \simeq \frac{Z/A}{Z'/A'} - 1. \tag{1.22}$$

For this reason, it is more convenient to have the pressure as the independent variable. In this way we avoid to make a Maxwell construction to estimate the pressure at which the transition from (A, Z) to (A', Z') occurs.

The BPS model is still widely used to determine the ground state of the outer crust. However, at that time the authors took the values of nuclear binding energy from the outdated phenomenological macroscopic model of Myers and Swiatecki [MS65]. Moreover, they did not take into account the zero-point vibration energy, Eq. (1.3). In the last decades, considerable efforts have been made to measure nuclear masses near the neutron drip line [LPT03], as well as theoretical developments were achieved to construct microscopic mass tables [Sam+02]. It is therefore important to reevaluate the ground state of the outer crust considering those experimental and theoretical advances. In this line, Haensel and Pichon studied the consequences of progress concerning the experimental determination of atomic masses in 1994 [HP94]. The authors found that the ground state of the outer crust can be determined exclusively by experimental masses in a fully model independent way up to $\rho_B \approx 10^{11}$ g/cm^3. From this density up to the neutron drip point, the phenomenological, liquid-drop based mass formula of Möller was used, the formalism of which is described in [MN88].

In the same spirit as [HP94], we calculate, in the following, the ground state of the outer crust using the present day knowledge on experimental masses of neutron rich nuclei [Hua+17; Wel+17] combined with state-of-the-art microscopic theoretical mass tables [GCP13].

1.1.3 Equilibrium composition and equation of state

We turn to the numerical results obtained applying the BPS method presented in 1.1.2. The ground state of the outer crust is calculated, beginning at $P = 3 \times 10^{-11}$, corresponding approximately to $n_B \approx 10^{-9}$ fm^{-3}, in order to ensure complete ionization and electron degeneracy. The pressure is increased from steps of $0.02P$ until the neutron drip point, defined by $\mu_n - m_n c^2 = 0$, is reached.

The ground-state composition and EoS of the outer crust of a cold non-accreting NS is reported in Table 1.1. The upper part of the table, $n_B < 3.84 \times 10^{-5}$ fm^{-3}, corresponding to $\rho_B < 6.39 \times 10^{10}$ g/cm^3, is exclusively determined by experimental data from the AME2016 [Hua+17]. Let us notice that the maximum mass density at which experimentally studied nucleus ^{80}Zn was present was found to be slightly lower in [HP94], $\rho_B = 5.44 \times 10^{10}$ g/cm^3. This is due to the fact that the determination of this value of density depends on the mass formula used, here HFB-24, for the neutron rich nuclides present in the bottom layers of the outer crust. From 3.84×10^{-5} fm^{-3}, matter becomes so neutron rich that the nuclear masses cannot be measured experimentally for now, thus a model dependence is expected to arise because the nuclear masses have to be extrapolated from laboratory nuclei. The nuclear mass model used to calculated the ground state here is HFB-24 [GCP13], constructed from the BSk24 functional following the Hartree-Fock-Bogoliubov method [Sam+02]. The BSk24 functional is part of a family of functionals labeled BSk22 to BSk26, consisting of unconventional effective Skyrme forces with extra t_4 and t_5 terms that behave as density-dependent generalizations of the usual t_1 and t_2 terms present in traditional Skyrme forces. The functionals BSk22-

element	Z	N	Y_p	$n_{B,max}$ (fm^{-3})	P_{max} (MeV/fm^3)	$\mu_n - m_n c^2$ (MeV)	μ_e (MeV)
^{56}Fe	26	30	0.4643	4.97×10^{-9}	3.40×10^{-10}	-8.96	0.95
^{62}Ni	28	34	0.4516	1.56×10^{-7}	4.09×10^{-8}	-8.26	2.57
^{64}Ni	28	36	0.4375	8.07×10^{-7}	3.60×10^{-7}	-7.52	4.34
^{66}Ni	28	38	0.4242	9.27×10^{-7}	4.16×10^{-7}	-7.46	4.50
^{86}Kr	36	50	0.4186	1.85×10^{-6}	1.03×10^{-6}	-7.01	5.63
^{84}Se	34	50	0.4048	6.85×10^{-6}	5.64×10^{-6}	-5.87	8.59
^{82}Ge	32	50	0.3902	1.67×10^{-5}	1.77×10^{-5}	-4.82	11.41
^{80}Zn	30	50	0.3750	3.84×10^{-5}	5.10×10^{-5}	-3.58	14.86
^{78}Ni	28	50	0.3590	6.68×10^{-5}	1.01×10^{-4}	-2.63	17.61
^{126}Ru	44	82	0.3492	7.52×10^{-5}	1.12×10^{-4}	-2.47	18.15
^{124}Mo	42	82	0.3387	1.21×10^{-4}	2.04×10^{-4}	-1.54	21.05
^{122}Zr	40	82	0.3279	1.56×10^{-4}	2.75×10^{-4}	-1.03	22.69
^{121}Y	39	82	0.3223	1.63×10^{-4}	2.84×10^{-4}	-0.98	22.86
^{120}Sr	38	82	0.3167	1.95×10^{-4}	3.52×10^{-4}	-0.60	24.12
^{122}Sr	38	84	0.3115	2.37×10^{-4}	4.49×10^{-4}	-0.15	25.62
^{124}Sr	38	86	0.3065	2.56×10^{-4}	4.87×10^{-4}	0.00	26.14

Table 1.1: Ground state of the outer crust of a cold non-accreting neutron star. Experimental data from the 2016 Atomic Mass Evaluation [Hua+17] are used when available. Mass excesses of $^{77-79}$Co are taken from [Wel+17]. Experimental masses are supplemented with masses from microscopic HFB-24 theoretical mass table [GCP13] (lower part). The last line corresponds to the neutron drip point. The following quantities are reported in the table: the element, the atomic number Z, the neutron number N, the proton fraction $Y_p = Z/A$ (A is the number of nucleons), the maximum baryon density $n_{B,max}$ at which the nuclide is found, the associated pressure P_{max}, the neutron chemical potential minus rest mass $\mu_n - m_n c^2$, and the electron chemical potential μ_e.

26 were fitted to the 2353 experimental masses of the AME2012 [Aud+12] and differ mainly by their symmetry energy S, defined here as the difference between the energy per nucleon of pure neutron matter (PNM) e_{PNM} and the energy per nucleon of symmetric nuclear matter (SNM) e_{SNM},

$$S(n) = e_{PNM}(n) - e_{SNM}(n), \tag{1.23}$$

with n the density of nuclear matter. To a first approximation, $S(n) \simeq E_{sym}$, E_{sym} being the symmetry energy per nucleon at the saturation density of nuclear matter $n = n_{sat} \approx 0.16$ fm^{-3}. This quantity is constrained to 32, 31, 30, and 29 MeV for BSk22, BSk23, BSk24, and BSk25, respectively. For BSk26, $E_{sym} = 30$ MeV as well but the functional is fitted to the APR EoS of PNM [APR98], unlike BSk22-25 that are fitted to the stiffer LS2 EoS [LS08].

The first layer of the outer crust consists of a crystal lattice of ^{56}Fe, the mass per nucleon of which is the lowest among all nuclides. The sequence of nuclides is in good

agreement with the results of [HP94]. One can note the persistence of magic numbers $Z = 28$ and $N = 50$ at low density, and $Z = 82$ at higher density. In particular, in [HP94] the $N = 82$ shell is found from $\rho_B = 9.64 \times 10^{10}$ g/cm^3 to 4.32×10^{11} g/cm^3, point of neutron drip (see Table 3.1 of [HPY07]). It is explained in [HPY07] that the apparent strong effect of the $N = 82$ shell in the bottom layers could be an artifact of the extrapolation using the mass formula of [MN88] and that further investigations on nuclear shell structure in the vicinity of the neutron drip point were required. Here we find two additional layers of strontium ($N = 84$ and $N = 86$) with respect to [HP94] results, and the layer of ^{118}Kr before the neutron drip is not observed.
At high density, a thin layer of odd-mass nuclei ^{121}Y is found with the HFB-24 mass model. It is interesting since the possibility of having odd nuclei in the ground state of the outer crust was not considered in the original calculation of BPS [BPS71]. Also, it is reported in [Pea+18] that ^{79}Co is favored over ^{76}Ni, found for HFB-22 and HFB-25, in the case where the recent mass excess measurements of [Wel+17] are accounted for. This highlights the importance of measuring the mass of odd-nuclei. One could expect that the presence of odd-nuclei in the outer crust of NS leads to ferromagnetic phase transitions at low temperature. In return, it could generate a magnetic field and alter the existing field, and so the electron gas.
It can also be observed in Table 1.1 that the proton fraction $Y_p = Z/A$ always decreases with increasing depth. The neutronization of matter can be understood by the following reason. Neglecting the static-lattice energy as well as the zero-point quantum vibrations terms, we can write the zero-temperature Gibbs energy per nucleon as

$$g \simeq \frac{M'(A,Z)c^2 + V\varepsilon_e}{n_B V} + \frac{P}{n_B}. \tag{1.24}$$

Since the lattice does not contribute to the pressure, we have $P \simeq P_e = n_e\mu_e - \varepsilon_e$, yielding

$$g \simeq \frac{M'(A,Z)c^2}{A} + \frac{n_e}{n_B}\mu_e. \tag{1.25}$$

The charge neutrality is ensured in the unit cell, therefore $n_e/n_B = Z/A$ and we finally get

$$g \simeq \frac{M'(A,Z)c^2}{A} + \frac{Z}{A}\mu_e. \tag{1.26}$$

For $\rho_B \gg 10^{-7}$ g/cm^3, electrons are ultrarelativistic and the electron chemical potential is calculated by taking the derivative of Eq. (1.10),

$$\mu_e = \frac{\partial \varepsilon_e}{\partial n_e} = \frac{3}{4}\hbar c(3\pi^2)^{1/3} n_e^{4/3}. \tag{1.27}$$

Therefore, the electron chemical potential μ_e scales as $P^{1/4}$ ($P \propto n_e^{4/3}$). Then it appears that, with increasing pressure, it is energetically favorable to decrease the proton fraction $Y_p = Z/A$ in order to compensate the increase in the term $M'(A,Z)c^2/A$.
The neutron chemical potential monotonously increases with increasing density and at $n_B = 2.56 \times 10^{-4}$ fm^{-3}, corresponding to $P = 4.87 \times 10^{-4}$ MeV/fm^{-3}, the neutron drip is finally reached. It should be mentioned that the neutron drip density as well as pressure depend on the mass model, here chosen to be HFB-24.

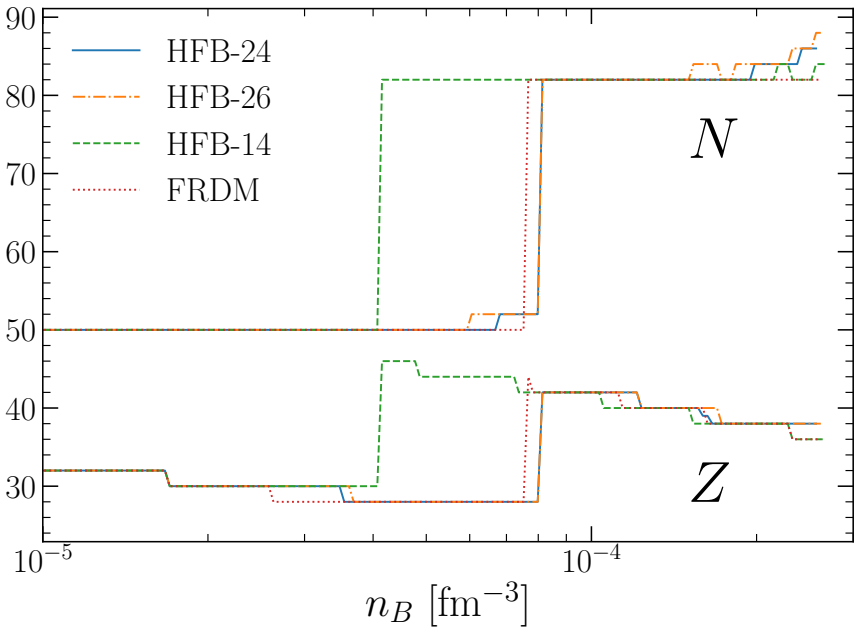

Figure 1.1: Variation with baryon density n_B of the equilibrium value of atomic number Z and neutron number N in the bottom layers of the outer crust for four different models: HFB-24, HFB-26 [GCP13], HFB-14 [GSP07], and the FRDM [Mol+95].

The model dependence of the composition in the bottom layers of the outer crust (bottom part of Table 1.1) can be seen in Figure 1.1, where we represent the proton number Z and the neutron number N as a function of the baryon density n_B for four different mass models that reproduce with comparable accuracy the present experimental mass information: HFB-14 [GSP07], HFB-24, HFB-26 [GCP13], and the FRDM [Mol+95] that supplement the experimental data. The model dependence is observed from $n_B \approx 2.5 \times 10^{-5}$ fm^{-3}, where the experimental mass data are not available. We recover similar sequences of nuclides with the different mass models, with the strong shell effect associated to $N = 50$ at low density and $N = 82$ in the bottom layers. A thin layer with $N = 52$ is also found for HFB-24 and HFB-26 just before the transition to $N = 82$. While this transition occurs in the vicinity of $\approx 8 \times 10^{-5}$ fm^{-3} for HFB-24, HFB-26, and the FRDM, it is found to happen at approximately 4×10^{-5} fm^{-3} for HFB-14. Different nuclides are found close to the neutron drip, depending on the model: ^{124}Sr is found for HFB-24, ^{126}Sr for HFB-26, ^{120}Kr for HFB-14, and ^{122}Kr for the FRDM. The neutron drip density n_{ND} and pressure P_{ND} slightly depends on the model as well. These values are reported in Table 1.2.

The variation of pressure with baryon density, namely the EoS, is shown in Fig. 1.2 for the four mass models. The selected models give the same value of pressure up to $\approx 2.5 \times 10^{-5}$ fm^{-3}, as it is the case for the composition. At higher densities, we can perceive the small effect of the model, in particular at the transitions from a layer to

model	element	Z	N	n_{ND} (fm^{-3})	P_{ND} (MeV/fm^3)
HFB-24	^{124}Sr	38	86	2.56×10^{-4}	4.87×10^{-4}
HFB-26	^{126}Sr	38	88	2.62×10^{-4}	4.91×10^{-4}
HFB-14	^{120}Kr	36	84	2.67×10^{-4}	5.01×10^{-4}
FRDM	^{122}Kr	36	82	2.62×10^{-4}	4.99×10^{-4}

Table 1.2: Chemical element, atomic number Z, neutron number N, density n_{ND}, and pressure P_{ND} at the neutron drip point for four different mass models: HFB-24, HFB-26 [GCP13], HFB-14 [GSP07], and the FRDM [Mol+95].

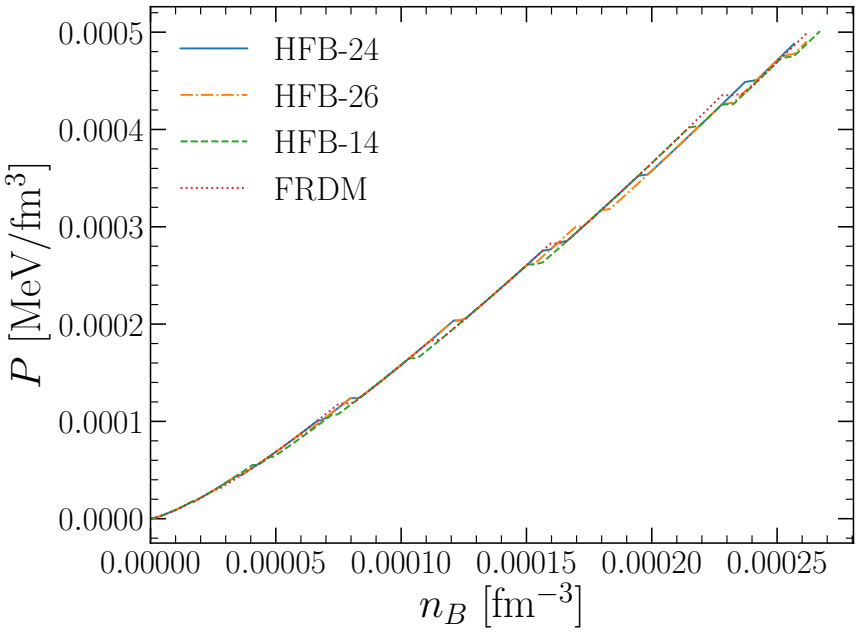

Figure 1.2: Variation with baryon density n_B of pressure P for four different models: HFB-24, HFB-26 [GCP13], HFB-14 [GSP07], and the FRDM [Mol+95].

another at which the pressure stays constant, but where a discontinuity is observed in the density.

1.2 Ground state of the inner crust

The neutron drip marks the onset of the inner crust, which is a system that cannot be reproduced in the laboratory since the dripped neutrons would evaporate, while they stay confined in the WS cell due the gravitational pressure. For this reason, the equilibrium composition and so the EoS in the inner crust are fully model dependent.

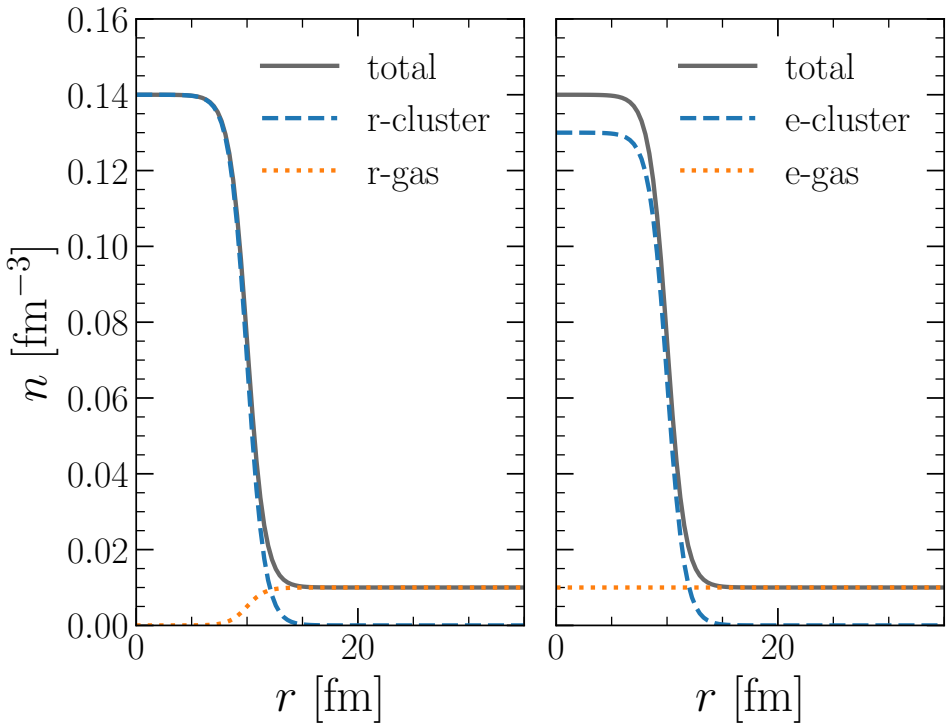

Figure 1.3: Wood-Saxon density profiles, for arbitrary values, within a WS cell in the free neutron regime. Blue dashed lines correspond to the cluster density (left, r-cluster; right, e-cluster), and orange dotted lines to the gas density. The total density profile is represented in gray solid lines.

This section deals with the determination of the ground state of the inner crust. In 1.2.1, we present the metamodeling of the infinite nuclear matter EoS here used to calculate the energy of the neutron gas, and extended to finite nuclei within the so-called compressible liquid drop (CLD) approximation so as to describe the cluster energetics. The derivation of the system of equilibrium equations for the determination of inner-crust ground state is detailed in 1.2.2. The numerical method as well as results are presented afterwards, in 1.2.3. In 1.2.4 we add Strutinsky shell corrections on top of the CLD energy as an attempt to recover magic numbers in the free neutron regime. Nonspherical pasta phases in the bottom layers of the inner crust are considered in 1.2.5. Finally, the phase transition from the solid crust to the liquid core is investigated in 1.2.6.

1.2.1 Modeling the nuclear energy

Once the neutron dripline is reached, neutron start to drip out of nuclei but stay confined in the WS cell because of the gravitational pressure, whereas they would have been emitted in the laboratory. In the regime of the inner crust, we thus have, in each unit cell, a cluster immersed in an electron sea, and an ambient neutron gas.

There is an ambiguity regarding the characterization of the cluster-gas interface. One should ask whether the neutron gas penetrate the cluster or not. Hence, two classical representations can be introduced, namely the r-cluster and e-cluster representations [Pap+13], to interpret the distribution of the N_{WS} neutrons and Z_{WS} protons in the unit cell. In the former, the cluster occupy a volume at the center of the cell and is surrounded by the neutron gas. Evidently, there is a thin region where cluster and gas overlap given the fact that a sharp interface would be unrealistic. The r-cluster representation naturally emerges in the local density approximation in density functional theory. Indeed, if the energy is expressed as a function of the local density, then the cluster corresponds to the dense part and the gas to the dilute one. This interpretation is used in most of the calculations at finite temperature to model supernovae, see for example the renowned Lattimer and Swesty EoS [LS91]. In the e-cluster representation, the gas penetrate the cluster. This interpretation appears spontaneously in single-particle developments. Indeed, in very neutron-rich clusters, beyond the neutron dripline, the bound states are occupied as well as the resonant and continuum states. All the unbound single-particle states that are occupied thus represents the neutron gas, characterized by a quasihomogeneous spatial distribution, the continuum wave functions being very similar to plane waves. The difference between the two representations is illustrated in Fig. 1.3. The cluster and gas density profiles, described by Woods-Saxon profiles with arbitrary values, are plotted along the WS cell radius in the r-cluster representation (left) and e-cluster representation (right). Woods-Saxon profiles are known to give a good description of medium-mass and heavy nuclei density profiles, and are commonly used in Thomas-Fermi (TF) and extended Thomas-Fermi (ETF) calculations [Ons+08; Pea+18]. In both representations, the total density profile (solid gray line) is the same. One can benefit from the advantage of both representations through the simple geometric relations

$$A_e = A\left(1 - \frac{n_g}{n_0}\right), \quad Z_e = A\left(1 - \frac{n_{g,p}}{n_{0,p}}\right), \tag{1.28}$$

where A_e (Z_e) is the number of nucleons (protons) in the e-cluster, A (Z) the number of nucleons (protons) in the r-cluster, n_g ($n_{g,p}$) the total (proton) gas density, and n_0 ($n_{0,p}$) the average total (proton) density inside the cluster. Since we do not consider the possibility of proton drip in the inner crust, we have $n_{g,p} = 0$, yielding $Z_e = Z$ and implying that the total gas density is equal to that of the neutron gas. Indeed, while free protons are expected at non-zero temperature, their presence at zero temperature remains uncertain [BBP71] and depends on the nuclear model. For some models, the proton drip could set in the very bottom layers of the crust, the classical condition for which is $\mu_p = U_p + m_p c^2$, where U_p corresponds to the proton single-particle field at the cell surface [Pea+18]. However, if nonspherical shapes are considered then it is found that protons remain in the cluster for most models.

At zero temperature, we write the WS cell energy E_{WS} in the r-cluster representation as

$$E_{WS} = E_{cl} + V_{WS}\varepsilon_e + (V_{WS} - V_{cl})\varepsilon_g + Z_{WS}(m_p - m_n)c^2 + A_{WS}m_n c^2 \tag{1.29}$$

where ε_g represents the energy density of the surrounding neutron gas of density n_g, $V_{cl} = A/n_0$ the volume of the cluster, V_{WS} that of the WS cell, and E_{cl} the energy of

the cluster. The total number of protons Z_{WS} and nucleons A_{WS} inside the WS cell are given respectively by

$$Z_{WS} = A\frac{1-I}{2} \quad \text{and} \quad A_{WS} = A\left(1 - \frac{n_g}{n_0}\right) + n_g V_{WS}. \tag{1.30}$$

Let us notice that the number of protons inside the cell remains an integer number, as in the outer crust, unlike the number of neutrons that is noninteger because of the outside neutron gas.

As for the bottom layers of the outer crust, the determination of the ground state of the inner crust is fully model dependent. Therefore, the two necessary ingredients of the WS cell energy are the equation of state of PNM, and the energy of the cluster, which will be treated in the CLD approximation introduced by Baym, Bethe, and Pethick (BBP) in their pioneering work [BBP71].

1.2.1.1 Metamodeling of homogeneous nuclear matter

The ambient neutron gas in the WS cell is treated as homogeneous nuclear matter. In this limit, a large number of nucleons $A \longrightarrow \infty$ is contained in a large box. The system is entirely characterized by the neutron density n_n and the proton density n_p. Let us also introduce the total density $n = n_n + n_p$ and the asymmetry $\delta = (n_n - n_p)/n$. Two limit cases can be distinguished: pure neutron matter, where $n_p = 0$, and symmetric nuclear matter, where $n_n = n_p$. Beta-equilibrated matter corresponds to the matter inside the core of neutron stars and is treated in Section 1.3. Different methods have been proposed in order to evaluate the energy per nucleon of homogeneous nuclear matter. While considerable theoretical efforts have been devoted to ab initio approaches in the recent years [Gan+14], these calculations might become unreliable at suprasaturation densities. Also, the treatment of three-body forces, which are known to play a major role in the determination of the saturation properties of nuclear matter, remains a challenge [DHS16]. Another possibility is to derive the nuclear EoS from effective forces [Cha+98]. This second approach is very practical because of translational invariance but suffers from the possible introduction of artificial correlations among the parameter space. In the following we present the metamodeling technique [MHG18a; MHG18b]. As we will see, this technique allows to parametrize in a simple analytical way the energy per nucleon obtained in the different ab initio or effective approaches, as well as interpolate continuously between them. By largely exploring the parameter space of this metamodel (or model of models), constraints coming from experimental measurements can be directly implemented. Indeed, nuclear experiments give us knowledge on the properties of nuclear matter around the saturation density of symmetric nuclear matter n_{sat}, which is roughly the density of laboratory nuclei. For instance, the isoscalar Giant Monopole Resonance energy is correlated with the empirical parameter K_{sat}, which corresponds to the isoscalar modulus. The well-known nuclear EoS empirical parameters correspond in fact to the successive density derivatives of nuclear matter energy per particle of SNM and symmetry energy at saturation density, associated to the isoscalar (E_{sat}, K_{sat}, Q_{sat}, and Z_{sat}) and isovector channel (E_{sym}, L_{sym}, K_{sym}, Q_{sym}, and Z_{sym}), respectively. The

Parameter	Unit	N	SLy4	BSk24	BSk22	DD-MEδ	Average	Uncertainty
E_{sat}	MeV	0	-15.97	-16.05	-16.09	-16.12	-15.8	0.3
n_{sat}	fm^{-3}	1	0.1595	0.1578	0.1578	0.1520	0.155	0.005
K_{sat}	MeV	2	230	246	246	219	230	20
Q_{sat}	MeV	3	-363	-274.5	-276	-748	300	400
Z_{sat}	MeV	4	1587	1184	1190	3950	-500	1000
E_{sym}	MeV	0	32.01	30.00	32.00	32.35	32	2
L_{sym}	MeV	1	46.0	46.4	68.5	52.8	60	15
K_{sym}	MeV	2	-120	-38	13	-118	-100	100
Q_{sym}	MeV	3	521	711	563	846	0	400
Z_{sym}	MeV	4	-3197	-4031	-3174	-3545	-500	1000
m^*_{sat}/m			0.69	0.80	0.80	0.69	0.75	0.1
$\Delta m^*_{sat}/m$			-0.19	0.20	0.20	-0.17	0.1	0.1

Table 1.3: Empirical parameter and associated unit and derivative order N for SLy4 [Cha+98], BSk24, BSk22 [GCP13], and DD-MEδ [Roc+11] functionals. Average values and uncertainties extracted from experimental analysis are taken from [MHG18a].

symmetry energy is generally defined as

$$e^{sym}_{HM}(n) = \frac{1}{2}\frac{\partial^2 e_{HM}(n,\delta)}{\partial \delta^2}\bigg|_{\delta=0}, \tag{1.31}$$

where e_{HM} is the nuclear matter energy per nucleon in nuclear matter. In Table 1.3 are listed the value of each empirical parameter for the Skyrme-like SLy4 [Cha+98], BSk22, and BSk24 [GCP13], and relativistic DD-MEδ [Roc+11] functionals. Average values and associated uncertainties extracted from experimental analysis are also provided. It can be seen that the isovector parameters are in general less known with respect to the isoscalar ones for the same derivative order. For instance, the relative uncertainty on K_{sym} is about 100% while that of K_{sat} is less than 10%. It should also be stressed that high-order parameters $Q_{sat(sym)}$ and $Z_{sat(sym)}$ are poorly constrained by nuclear experiments.
The empirical parameters can be used in a Taylor expansion to estimate the nuclear matter EoS analytically up to $n \approx 2 - 3n_{sat}$ [MHG18a; MHG18b]. Limiting us to derivative order $N = 2$, we obtain

$$e^{N=2}_{HM}(n,\delta) = E_{sat} + \frac{1}{2}K_{sat}x^2 + \delta^2(E_{sym} + L_{sym}x + \frac{1}{2}K_{sym}x^2), \tag{1.32}$$

with $x = (n - n_{sat})/(3n_{sat})$ a function of the density. However, we should stress already that $N = 2$ is not sufficient for describing the EoS at subsaturation densities, and even less for suprasaturation densities. High-order parameters $Q_{sat(sym)}$ and $Z_{sat(sym)}$ are essential and carry the largest uncertainty as far as the bulk part of the EoS is concerned.

In a mean field approach, we can treat nucleons as independent particles, thus the kinetic part of the energy per particle of nuclear matter is given by the same functional form as a nonrelativistic Fermi gas (FG), that is

$$t_{HM}^{FG}(n,\delta) = \frac{1}{2} t_{sat}^{FG}(1+3x)^{2/3}\left[(1+\delta)^{5/3}\frac{m}{m_n^*} + (1-\delta)^{5/3}\frac{m}{m_p^*}\right], \tag{1.33}$$

where $t_{sat}^{FG} = 3\hbar^2/(10m)(3\pi^2/2)^{2/3} n_{sat}^{2/3}$ is the kinetic energy of SNM at the saturation density, $m = (m_n + m_p)/2$ is the mean nucleon mass, and m_n^* (m_p^*) is the neutron (proton) effective mass. The Landau effective mass is introduced in order to take into account for the in-medium nuclear interaction that alters the mass of nucleons. It can be parametrized as ($q = n, p$)

$$\frac{m}{m_q^*} = \sum_{\alpha=0}^{1} m_{q,\alpha}(\delta)\frac{x^\alpha}{\alpha!} = 1 + (\kappa_{sat} + \tau_3\kappa_{sym}\delta)(1+3x), \tag{1.34}$$

with $\tau_3 = 1$ ($\tau_3 = -1$) for neutrons (protons). Two additional parameters κ_{sat} and κ_{sym}, related to the effective mass m_{sat}^* and isospin splitting Δm_{sat}^* at saturation density, are then introduced. They are defined at $n = n_{sat}$ as

$$\kappa_{sat} = \frac{m}{m_{sat}^*} - 1, \tag{1.35}$$

$$\kappa_{sym} = \frac{1}{2}\left(\frac{m}{m_n^*} - \frac{m}{m_p^*}\right). \tag{1.36}$$

In principle, it is possible to reproduce any EoS model with a Taylor expansion, considering an infinite number of parameters, $N \to \infty$, however the convergence would be very slow. In order to fasten the series convergence, one can add extra functional dependencies, which correspond to the true EoS in the limit of simplistic cases (independent particles, zero density limit), but which allow, by judicious choices of empirical parameters, to reproduce with precision realistic functionals. In this regard, the $\delta^{5/3}$ dependence is added by decomposing the energy per particle into a potential and kinetic part, yielding

$$e_{HM}^N(x,\delta) = t_{HM}^{FG}(n,\delta) + v_{MM}^N(n,\delta), \tag{1.37}$$

where v_{MM}^N is the potential energy per particle expressed as a Taylor expansion in the parameter x at $n = n_{sat}$,

$$v_{MM}^N(n,\delta) = \sum_{\alpha\geq 0}^{N}(v_\alpha^{is} + \delta^2 v_\alpha^{iv})\frac{x^\alpha}{\alpha!}. \tag{1.38}$$

The quadratic approximation for the isospin dependence of the potential energy has been made in Eq. (1.38), as suggested by microscopic calculations in [Vid+09]. The coefficients v_α^{is} and v_α^{iv} are mapped to the empirical parameters following

$$v_\alpha^{is} = \left.\frac{\partial^\alpha e_{HM}}{\partial x^\alpha}\right|_{n=n_{sat},\delta=0} \quad \text{and} \quad v_\alpha^{iv} = \left.\frac{\partial^\alpha e_{HM}^{sym}}{\partial x^\alpha}\right|_{n=n_{sat},\delta=0}, \tag{1.39}$$

yielding the isoscalar parameters:

$$
\begin{aligned}
v_0^{is} &= E_{sat} - t_{sat}^{FG}(1+\kappa_{sat}), && (1.40)\\
v_1^{is} &= -t_{sat}^{FG}(2+5\kappa_{sat}), && (1.41)\\
v_2^{is} &= K_{sat} - 2t_{sat}^{FG}(-1+5\kappa_{sat}), && (1.42)\\
v_3^{is} &= Q_{sat} - 2t_{sat}^{FG}(4-5\kappa_{sat}), && (1.43)\\
v_4^{is} &= Z_{sat} - 8t_{sat}^{FG}(-7+5\kappa_{sat}), && (1.44)
\end{aligned}
$$

and isovector parameters:

$$
\begin{aligned}
v_0^{iv} &= E_{sym} - \frac{5}{9}t_{sat}^{FG}[1+(\kappa_{sat}+3\kappa_{sym})], && (1.45)\\
v_1^{iv} &= L_{sym} - \frac{5}{9}t_{sat}^{FG}[2+5(\kappa_{sat}+3\kappa_{sym})], && (1.46)\\
v_2^{iv} &= K_{sym} - \frac{10}{9}t_{sat}^{FG}[-1+5(\kappa_{sat}+3\kappa_{sym})], && (1.47)\\
v_3^{iv} &= Q_{sym} - \frac{10}{9}t_{sat}^{FG}[4-5(\kappa_{sat}+3\kappa_{sym})], && (1.48)\\
v_4^{iv} &= Z_{sym} - \frac{40}{9}t_{sat}^{FG}[-7+5(\kappa_{sat}+3\kappa_{sym})], && (1.49)
\end{aligned}
$$

Let us notice from Eq. (1.38) that the energy per particle does not converge to zero at zero density. This artifact, arising from the nature of the series expansion, can be fixed by introducing an exponential correction $u_\alpha^N(x)$ in the potential energy,

$$
v_{MM}^N(n,\delta) = \sum_{\alpha\geq 0}^{N}(v_\alpha^{is}+\delta^2 v_\alpha^{iv})\frac{x^\alpha}{\alpha!}u_\alpha^N(x), \tag{1.50}
$$

the expression of which is

$$
u_\alpha^N(x) = 1-(-3x)^{N+1-\alpha}\exp(-b(1+3x)), \tag{1.51}
$$

where we have introduced an extra low-density parameter b. It was shown in [Ant+19] that for most applications this parameter can be fixed to a constant, $b = 10\ln(2)$.

Let us now turn to the derivatives of the energy. The expression of the symmetry energy, Eq. (1.31), reads

$$
e_{HM}^{sym}(n) = \frac{5}{9}t_{sat}^{FG}(1+3x)^{2/3}\left[1+(\kappa_{sat}+3\kappa_{sym})(1+3x)\right] + \sum_{\alpha\geq 0}^{N} v_\alpha^{iv}\frac{x^\alpha}{\alpha!}u_\alpha^N(x). \tag{1.52}
$$

For the chemical potential, we have

$$
\mu_{HM,q}(n,\delta) = e_{HM}^N + \frac{1+3x}{3}\left(\frac{\partial e_{HM}^N}{\partial x}\right)_\delta + (\tau_3-\delta)\left(\frac{\partial e_{HM}^N}{\partial \delta}\right)_x + m_q c^2, \tag{1.53}
$$

The complete analytical expression of $\mu_{HM,q}$ is given in Appendix B. Finally, the pressure can be calculated through

$$
P_{HM} = \sum_{q=n,p} n_q(\mu_{HM,q}(n,\delta)-m_q c^2) - n e_{HM}^N(n,\delta). \tag{1.54}
$$

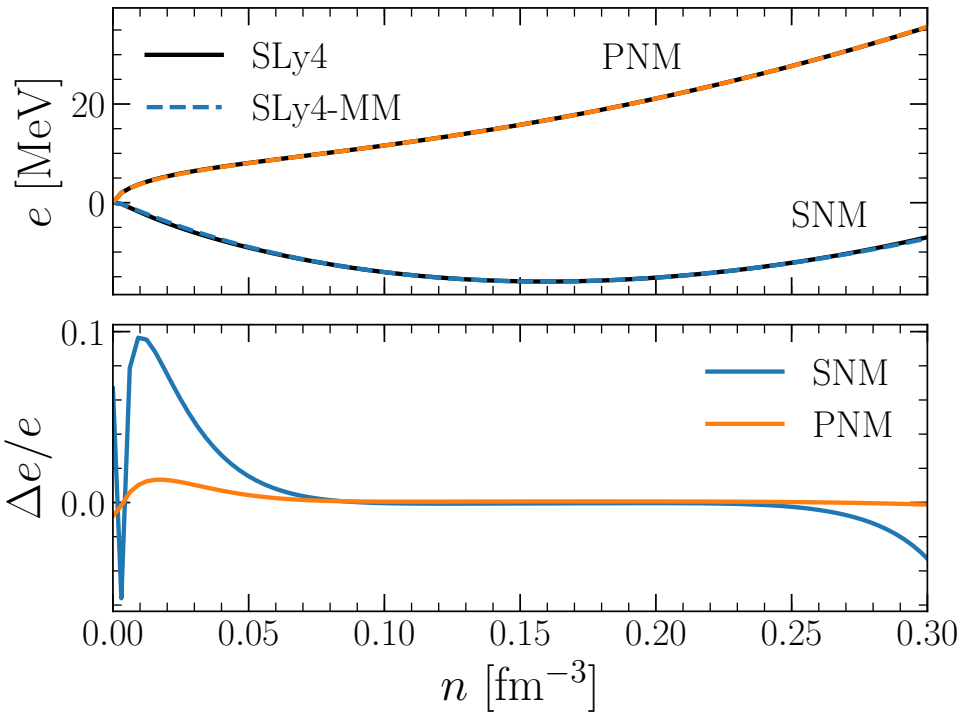

Figure 1.4: Energy per nucleon as a function of density for symmetric nuclear matter, $\delta = 0$, and pure neutron matter, $\delta = 1$ (upper panel), and the associated relative error $\Delta e/e = (e_{MM} - e)/e$ (lower panel) for the SLy4 functional, with $N = 4$ for the metamodel. In the top panel, black solid lines (dashed lines) correspond to the calculation with the exact functional (metamodel).

There are two main advantages that come with the metamodeling technique. Firstly, It is flexible enough to reproduce the different existing energy functional of nuclear matter with very good accuracy up to $n \approx 2 - 3n_{sat}$, and even higher densities with a proper redefinition of the third and fourth order parameters [MHG18a]. Since very often the parameters of the model to be mimicked do not coincide with the empirical parameters, we derive the latter by calculating the derivatives of the energy per particle in nuclear matter at saturation density, following Eq. (1.39). In Fig. 1.4 is demonstrated the accuracy of the metamodeling technique for the SLy4 [Cha+98] functional with a Taylor expansion order $N = 4$. In the top panel, the energy per nucleon is calculated using the metamodeling technique (dashed lines) and the exact functional (black solid lines). A tiny deviation is observed at low density for the SNM, but overall a very good agreement is observed between the metamodel (labeled "SLy4-MM") and the exact functional (labeled "SLy4"). In the lower panel the relative error is represented for SNM and PNM. We can see that the error goes up to 10% for SNM at $n \approx 0.01$ fm^{-3} and rapidly drops to 0% at $n \approx 0.07$ fm^{-3}. At $n \approx 2n_{sat}$, a deviation appears due the extrapolation far from the saturation point. The deviation at low density can be reduced

by adjusting the parameter b entering in the low-density correction, Eq. (1.51) [Ant+19]. However, this small deviation is not expected to cause any issue for the determination of the inner crust ground state. Indeed, the relative error for PNM is lower that 2% at most, and, in the inner crust, the matter inside nuclei is very neutron rich and the ambient nucleon gas is exclusively constituted of free neutrons. This ability of mimicking existing realistic functionals will allow us to easily compare predictions of astrophysical observables of different popular models.
Another asset of the metamodeling technique is that no correlation is assumed a priori among the empirical parameters due to the nature of the series expansion. Therefore, all density dependences of the nuclear EoS can be explored. In addition, it allows us to vary each empirical parameter independently of the others to carry out complete statistical analysis using Bayesian inference.

1.2.1.2 From homogeneous nuclear matter to finite nuclei in the CLD approximation

We now turn to the modeling of the energy of clusters present in the inner crust of cold neutron stars. We propose to extend the metamodeling of infinite nuclear matter to nuclei in order to take into account their surface properties, within the CLD approximation, originally introduced in [BBP71]. This approach is expected to be less accurate than microscopic Hartree-Fock (HF) [NV73] or (ETF) [Ons+08] calculations since quantum effects are neglected, though it proved its quality in the past by giving surprisingly good results, see for example [BBP71; LS91; DH00; DH01]. In particular, it appears that most of the macroscopic observables related to neutron stars, such as masses and radii, are not very sensitive to the crust composition, thus a qualitative evaluation of it is sufficient in that case. The compressible liquid drop model (CLDM) comes with multiple advantages. It is very fast from the computational point of view since the energy does not require to be integrated all along the cell volume. For this reason, it is powerful for complete statistical analyses such as the one presented in the next chapter. It is also a model that is flexible, giving us the opportunity to account for different geometries for example, as we consider in 1.2.5. Last but not least, because of the artificial decomposition of the nuclear cluster as a bulk term, a surface term, and a Coulomb term, we are able to identify the contributions of the different terms. For all these reasons, the CLDM is considered as a suitable alternative to semiclassical ETF and microscopic HF treatments, that additionally does not suffer from technical complications such as the definition of boundary conditions [NS09].

In the CLD approximation, the energy of the cluster reads

$$E_{cl} = e_{HM}(n_0, I)A + E_{surf} + E_{Coul}, \tag{1.55}$$

where E_{surf} represents the nuclear surface energy, and E_{Coul} is the Coulomb energy, including the lattice correction and finite-size effects, written as follows in the WS approximation,

$$E_{Coul} = \frac{3}{5}\frac{e^2}{r_0^2}\eta_{Coul}(u)\frac{Z^2}{A^{1/3}} = \frac{3}{20}\frac{e^2}{r_0^2}\eta_{Coul}(u)A^{5/3}(1-I)^2, \tag{1.56}$$

with

$$\eta_{Coul}(u) = 1 - \frac{3}{2}u^{1/3} + \frac{1}{2}u, \tag{1.57}$$

a function of the volume fraction $u = n_e/n_{0,p}$, with $n_{0,p} = n_0(1-I)/2$ the average proton density inside cluster. Let us notice that, the factor $3/5 \times 3/2 = 9/10$ entering in the lattice term can be replaced by the Mandelung constant for a body-centered cubic lattice, $C_M = 0.895929255682$ (see Table 2.4 of [HPY07]).
The bulk term is taken from the metamodel, keeping the same empirical parameters as for the calculation of the neutron gas energy, thus insuring consistency between the crust and the core treatment. The bulk energy is evaluated at n_0, the average density inside the cluster, and I, its global asymmetry.

Let us now turn to the expression of the nuclear surface energy. Assuming that clusters are spherical, it is given by

$$E_{surf} = 4\pi r_0^2 A^{2/3}\sigma, \tag{1.58}$$

where $r_0 = (4\pi n_0/3)^{-1/3}$ is related to the cluster density n_0, and σ is the nuclear surface tension. The simplest parametrization of the surface tension one could use is a constant, $\sigma \approx 1.03$ MeV/fm^2, as in the liquid drop model. However, clusters in the inner crust are expected to be very neutron rich and it appears evident that the surface tension of very asymmetric nuclei should be different to that of symmetric nuclei. In addition, it does not account for the interaction of the nuclear surface with the outside neutron gas, yielding $\sigma \to 0$ as $I \to 1$. This leads us to consider another parametrization for σ which would depend on the asymmetry I and consider the interaction with the gas. It should be mentioned that the exact value of $\sigma(I)$ is model dependent, and the uncertainty is particularly important for extreme isospin values encountered in the inner crust. Indeed, no experimental data exist on the surface energy of nuclei beyond the dripline, which is in-medium modified by the presence of the neutron gas [DHM00]. We use the expression originally proposed by Ravenhall *et al.* [RPL83] on the basis of TF calculations at extreme isospin ratios, and later employed in different works on neutron star crust and supernovae modeling within the CLD approximation [LS91; NGL12; LRP93]:

$$\sigma(I) = \sigma_0 \frac{2^{p+1} + b_s}{Y_p^{-p} + b_s + (1-Y_p)^{-p}}, \tag{1.59}$$

with $\boldsymbol{S} = \{\sigma_0, b_s, p\}$ the parameter space associated to the surface energy. The parameter $\sigma_0 = \sigma(I=0)$ represents the surface tension of symmetric nuclei, and b_s and p are the parameters that govern the isospin dependence of the surface tension. The proton fraction is related to the asymmetry inside the cluster via $Y_p = (1-I)/2$. Following [NGL12], we add a curvature term with the aim of having a better description of the nuclear surface and so of the composition of the inner crust in the ground state. For spherical clusters, the curvature energy reads

$$E_{curv} = 8\pi r_0 A^{1/3}\sigma_c, \tag{1.60}$$

where σ_c is the curvature tension related to the surface tension σ, Eq. (1.59),

$$\sigma_c = \sigma \frac{\sigma_{0,c}}{\sigma_0}\alpha(\beta - Y_p), \tag{1.61}$$

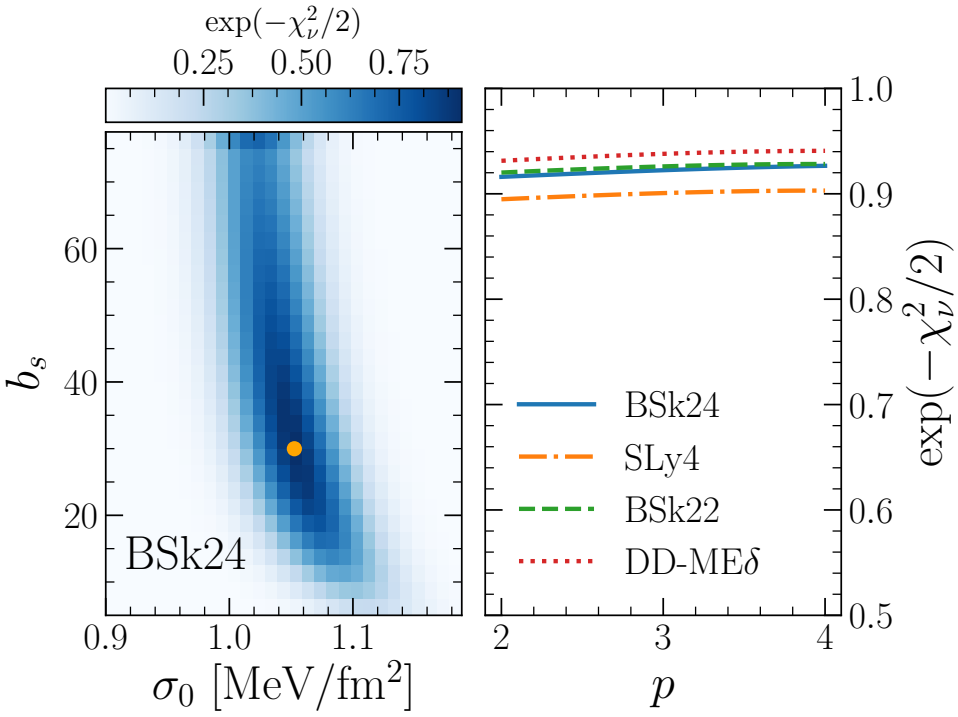

Figure 1.5: Blablabla

with $\alpha = 5.5$ as in [NGL12]. With the addition of the curvature energy comes two parameters added as extra dimensions to the surface parameter space, $\boldsymbol{S} = \{\sigma_0, b_s, \sigma_{0,c}, \beta, p\}$. For a given model of uniform matter, that is each given set of empirical parameters, the first four parameters can be fitted to experimental masses from the AME2016 [Hua+17] for a fixed value of the parameter p. This parameter is not adjusted as the other parameters because it controls the surface tension at extreme isospin whereas experimental data are available up to $I \approx 0.3$ only, thus we want to avoid poor extrapolations of σ. The value of p is selected around $p = 3$, which is the value used in the popular Lattimer and Swesty EoS [LS91]. We show in Fig. 1.6 the surface plus curvature energy per surface nucleon as a function of the asymmetry inside the cluster for two popular models, SLy4 [Cha+98] and DD-MEδ [Roc+11], in the CLD approximation. Different values for the parameter p are displayed in that figure. It is seen that p determines the behavior of the surface tension for extreme isospin values, and cannot be accessed from experimental nuclear physics data. In addition, since the selected popular models contain parameters that are adjusted to the same data, we cannot cannot consider their predictions at high isospin as reliable. For these reasons, we will keep p as a free parameter. In particular, from $I \approx 0.3$, we observe that a larger value of p leads to larger surface energy at fixed asymmetry. The model dependence of the surface tension is also observed in that figure and is particularly highlighted at low asymmetry where experimental measurements can still be performed.

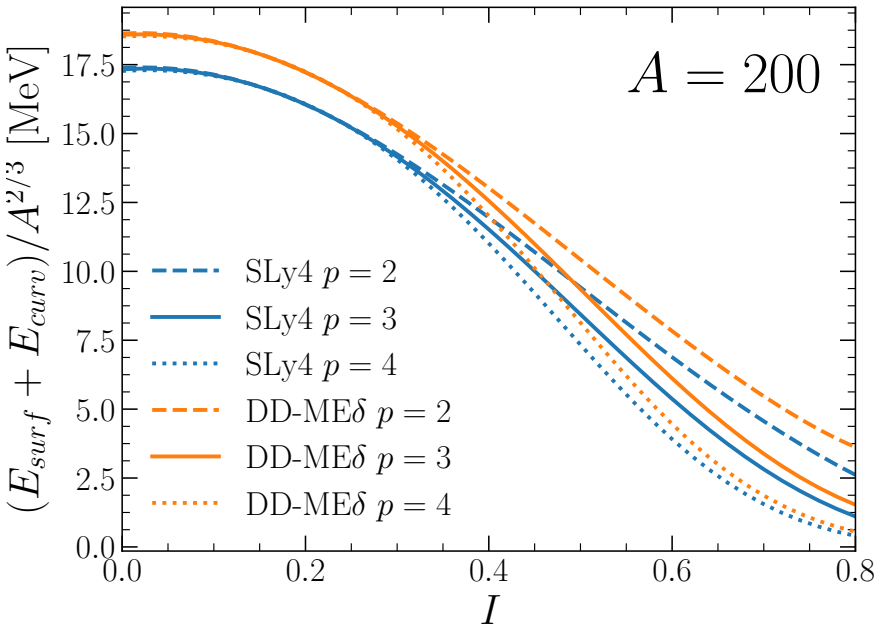

Figure 1.6: Variation with cluster asymmetry I of surface plus curvature energy per surface nucleon along the isobaric chain $A = 200$ for SLy4 [Cha+98] and DD-MEδ [Roc+11] CLDM at three selected values of parameter p: $p = 2$ (dashed lines), $p = 3$ (solid lines), and $p = 4$ (dotted lines).

Finally, we recall the final expression for the cluster binding energy in the CLD approximation,

$$\begin{aligned} E_{cl}(A, I, n_0, n_e) = \quad & e_{HM}(n_0, I)A \\ & + 4\pi r_0^2 A^{2/3}\sigma(I) + 8\pi r_0 A^{1/3}\sigma_c(I) \\ & + \frac{3}{20}\frac{e^2}{{r_0}^2}\eta_{Coul}(I, n_0, n_e)A^{5/3}(1-I)^2. \end{aligned} \tag{1.62}$$

Let us notice that the energy does not depend on the neutron gas density via the surface term, as in [BBP71]. This dependence is in fact implicitly accounted for in the chosen parametrization of the surface tension, suggested from microscopic calculations in the WS cell [RPL83].

1.2.2 Variational formalism

The variational method for the calculation of the inner crust ground state with the CLDM was introduced in the pioneering work of BBP in their classical paper [BBP71]. Since then, huge progress has been made in constraining the nucleon-nucleon (NN) effective interaction. For this reason, subsequent works using the same formalism with CLDM based on more realistic nuclear functionals followed. For instance we can mention

the popular calculations of Douchin and Haensel (DH) [DH00; DHM00] with the SLy4 effective force [Cha+98]. Following those works, we use the same variational method as BBP, and we present it in the following.

Using the Lagrange multipliers method, the ground state of the inner crust is obtained by minimizing the zero-temperature free energy density of the WS cell at fixed baryon density n_B under the condition of charge neutrality, $n_e = n_p$. The minimization is carried out with respect to the set of variables A, I, n_0, n_p, and n_g. Let us notice that, in principle, one should minimize the Gibbs free energy at constant pressure, as for the outer crust. However, it would be very heavy from the computational point of view to do so in the free neutron regime. Fortunately, it is demonstrated that the error introduced by minimizing at constant baryon density instead of pressure is negligible [Pea+12]. The auxiliary function to be minimized is defined as

$$\begin{aligned}\mathcal{L}(A, I, n_0, n_p, n_g) &= \frac{E_{WS}}{V_{WS}} - \mu n_B \\ &= \frac{E_{cl}}{V_{WS}} + \varepsilon_e + \left(1 - \frac{A}{n_0 V_{WS}}\right)\varepsilon_g \\ &\quad + n_p \Delta m_{pn} c^2 - n_B(\mu - m_n c^2),\end{aligned} \tag{1.63}$$

with $\Delta m_{pn} = m_p - m_n$ the difference between the proton and neutron mass, and μ the Lagrange multiplier.
The volume of the cell can be calculated as

$$V_{WS} = \frac{Z}{n_p} = \frac{A}{n_p}\frac{1-I}{2}, \tag{1.64}$$

and the baryon density is given by

$$\begin{aligned}n_B &= \frac{A_{WS}}{V_{WS}} \\ &= \frac{2n_p}{1-I}\left(1 - \frac{n_g}{n_0}\right) + n_g.\end{aligned} \tag{1.65}$$

Replacing these quantities in Eq. (1.63), it results

$$\begin{aligned}\mathcal{L}(A, I, n_0, n_p, n_g) &= \frac{2n_p}{A(1-I)}E_{cl} + \varepsilon_e + \left(1 - \frac{2n_p}{n_0(1-I)}\right)\varepsilon_g + n_p \Delta m_{pn} c^2 \\ &\quad - \frac{2n_p}{1-I}\left(1 - \frac{n_g}{n_0}\right)(\mu - m_n c^2) - n_g(\mu - m_n c^2).\end{aligned} \tag{1.66}$$

Let us first minimize with respect to A:

$$\begin{aligned}\left.\frac{\partial \mathcal{L}}{\partial A}\right|_{I,n_0,n_p,n_g} &= 0 \\ \frac{2n_p}{A(1-I)}\frac{\partial E_{cl}}{\partial A} - \frac{2n_p}{A^2(1-I)}E_{cl} &= 0 \\ \frac{\partial E_{cl}}{\partial A} - \frac{E_{cl}}{A} &= 0,\end{aligned} \tag{1.67}$$

which is equivalent to

$$\frac{\partial(E_{cl}/A)}{\partial A} = 0. \tag{1.68}$$

We can go trough this equation using the definition of the cluster energy, Eq. (1.62), yielding

$$\begin{aligned} -\frac{1}{3}\times 4\pi r_0^2\sigma A^{-4/3} - \frac{2}{3}\times 8\pi r_0\sigma_c A^{-5/3} + \frac{2}{3}\times\frac{3}{20}\frac{e^2}{r_0}\eta_{Coul}A^{-1/3}(1-I)^2 &= 0 \\ 4\pi r_0^2\sigma A^{2/3} + 2\times 8\pi r_0\sigma_c A^{1/3} - 2\times\frac{3}{20}\frac{e^2}{r_0}\eta_{Coul}A^{5/3}(1-I)^2 &= 0, \end{aligned}$$

or simply,

$$E_{surf} + 2E_{curv} = 2E_{Coul}. \tag{1.69}$$

This equation corresponds to the well-known Baym virial theorem with an additional curvature term with respect to the equation originally found in [BBP71]. It is interesting to notice that only the surface, the curvature, and the Coulomb energy are involved in this first equilibrium condition.

Minimizing with respect to the neutron gas density n_g, one obtains:

$$\begin{aligned} \left.\frac{\partial\mathcal{L}}{\partial n_g}\right|_{A,I,n_0,n_p} &= 0 \\ \left(1-\frac{2n_p}{n_0(1-I)}\right)\frac{\partial\varepsilon_g}{\partial n_g} + \frac{2n_p}{n_0(1-I)}(\mu - m_nc^2) - (\mu - m_nc^2) &= 0, \end{aligned} \tag{1.70}$$

giving us the expression of the Lagrange multiplier, which can be identified with the chemical potential of the gas, including the rest mass energy,

$$\mu = \frac{\partial\varepsilon_g}{\partial n_g} + m_nc^2 \equiv \mu_g. \tag{1.71}$$

We now turn to the minimization with respect to average cluster density n_0:

$$\begin{aligned} \left.\frac{\partial\mathcal{L}}{\partial n_0}\right|_{A,I,n_p,n_g} &= 0 \\ \frac{2n_p}{A(1-I)}\frac{\partial E_{cl}}{\partial n_0} + \frac{2n_p}{n_0^2(1-I)}\varepsilon_g - \frac{2n_pn_g}{n_0^2(1-I)}(\mu - m_nc^2) &= 0 \\ \frac{n_0^2}{A}\frac{\partial E_{cl}}{\partial n_0} - n_g(\mu - m_nc^2) + \varepsilon_g &= 0. \end{aligned} \tag{1.72}$$

Using well-known thermodynamical relations, we define $P_{cl} \equiv (n_0^2/A)(\partial E_{cl}/\partial n_0)$, and $P_g = n_g(\mu_g - m_nc^2) - \varepsilon_g$. Therefore, Eq. (1.72) simply results in

$$P_{cl} = P_g, \tag{1.73}$$

which can be interpreted as a pressure equilibrium condition between the cluster and the outside neutron gas. We can derive the expression of the cluster pressure from the CLD energy, Eq. (1.62), yielding

$$P_{cl} = P_{HM}(n_0, I) - \frac{2}{3}n_0\frac{E_{surf}}{A} - \frac{1}{3}n_0\frac{E_{curv}}{A} + n_0\frac{E_{coul}(u=0)}{A}\left(\frac{2}{3} + \frac{1}{2}u^{1/3} - \frac{1}{2}u\right). \tag{1.74}$$

The minimization with respect to the global asymmetry inside the cluster I yields

$$\begin{aligned} \left.\frac{\partial \mathcal{L}}{\partial I}\right|_{A,n_0,n_p,n_g} &= 0 \\ \frac{2n_p}{(1-I)^2}\left(\frac{E_{cl}}{A}+\frac{1-I}{A}\frac{\partial E_{cl}}{\partial I}-\frac{\varepsilon_g}{n_0}-\left(1-\frac{n_g}{n_0}\right)(\mu-m_nc^2)\right) &= 0 \\ \frac{E_{cl}}{A}+\frac{1-I}{A}\frac{\partial E_{cl}}{\partial I}-\frac{\varepsilon_g}{n_0}-\left(1-\frac{n_g}{n_0}\right)(\mu-m_nc^2) &= 0, \end{aligned} \tag{1.75}$$

resulting in

$$\frac{E_{cl}}{A}+\frac{1-I}{A}\frac{\partial E_{cl}}{\partial I}+\frac{P_g}{n_0}=\mu-m_nc^2. \tag{1.76}$$

Due to the presence of the outside neutron gas, the neutron chemical potential of the cluster is modified with respect to the usual expression in the vacuum $\mu_n^{vac}=\partial E_{cl}/\partial N$. We define the neutron and proton chemical potential of the cluster as

$$\mu_p^{cl}=\left.\frac{\partial E_{cl}}{\partial Z}\right|_N+m_pc^2 \quad \text{and} \quad \mu_n^{cl}=\left.\frac{\partial E_{cl}}{\partial N}\right|_Z+\frac{P_g}{n_0}+m_nc^2, \tag{1.77}$$

where the derivatives are taken at constant n_0, n_p, and n_g. Consequently, we can work out Eq. (1.76) to find a chemical equilibrium conditions between the neutrons of the cluster and those of the gas,

$$\mu_n^{cl}=\mu_g. \tag{1.78}$$

Finally, we minimize the auxiliary function, Eq. (1.63) with respect to the proton density n_p inside the WS cell,

$$\begin{aligned} \left.\frac{\partial \mathcal{L}}{\partial n_p}\right|_{A,I,n_0,n_g} &= 0 \\ \frac{E_{cl}}{A}+\frac{n_p}{A}\frac{\partial E_{cl}}{\partial n_p}+\frac{1-I}{2}\left(\frac{\partial \varepsilon_e}{\partial n_p}+\Delta m_{pn}c^2\right)-\frac{\varepsilon_g}{n_0}-\left(1-\frac{n_g}{n_0}\right)(\mu-m_nc^2) &= 0. \end{aligned} \tag{1.79}$$

By identifying common terms with Eq. (1.75), we recover the well-known beta equilibrium condition,

$$\frac{2}{A}\left(\frac{\partial E_{cl}}{\partial I}-\frac{n_p}{1-I}\frac{\partial E_{cl}}{\partial n_p}\right)-\Delta m_{pn}c^2=\frac{\partial \varepsilon_e}{\partial n_p}, \tag{1.80}$$

or in terms of chemical potentials,

$$\mu_n^{cl}=\mu_p^{cl}+\mu_e+\Delta\mu, \tag{1.81}$$

where $\Delta\mu$ represents the modification due to the excluded volume interaction with the neutron gas, and the electrostatic interaction between protons in the cluster and the background electrons. It is given by

$$\Delta\mu=\frac{P_g}{n_0}+\frac{2}{A(1-I)}n_p\frac{\partial E_{Coul}}{\partial n_p}. \tag{1.82}$$

One can remark that only the Coulomb energy enters in the derivative with respect to the proton density n_p. This derivative can be evaluated analytically from Eq. (1.56) as

$$\frac{\partial E_{Coul}}{\partial n_p} = \frac{3}{20}\frac{e^2}{r_0^2}A^{5/3}(1-I)\frac{1}{n_0}\left(1-\left(\frac{2n_p}{n_0(1-I)}\right)^{-2/3}\right). \tag{1.83}$$

Finally, a possible set of mechanical and chemical equilibrium equations is

$$\frac{\partial(E_{cl}/A)}{\partial A} = 0, \tag{1.84}$$

$$\frac{n_0^2}{A}\frac{\partial E_{cl}}{\partial n_0} = P_g(n_g), \tag{1.85}$$

$$\frac{E_{cl}}{A} + \frac{1-I}{A}\frac{\partial E_{cl}}{\partial I} + \frac{P_g(n_g)}{n_0} = \mu_g(n_g) - m_n c^2, \tag{1.86}$$

$$\frac{2}{A}\left(\frac{\partial E_{cl}}{\partial I} - \frac{n_p}{1-I}\frac{\partial E_{cl}}{\partial n_p}\right) - \Delta m_{pn}c^2 = \mu_e(n_p), \tag{1.87}$$

or, equivalently Eqs. (1.69), (1.73), (1.78), and (1.81), respectively. This system of four coupled differential equations can be solved numerically, as explained in 1.2.3.1, in order to obtain the equilibrium composition and so the EoS in the free neutron regime. Let us mention that taking alternatives set of variables leads to the same equilibrium equations [HPY07; Viñ+17].

1.2.3 Results

We now turn to the results of the minimization. The building of the numerical code is presented first and the numerical results, such as the ground-state composition and EoS of the inner crust, afterwards.

1.2.3.1 Numerical code

During the thesis, an open-source C library, NSEoS, has been built in relation to the physics of NS [Car17a]. Here we focus on the numerical methods used to solve the inner crust equilibrium equations in order to estimate the composition and EoS in the free neutron regime. Those methods can be found in the module `crust` of the library.

The ground state of the inner crust at baryon density n_B is determined by solving numerically the system of four coupled differential equations, Eqs. (1.84), (1.85), (1.86), and (1.87). To do so, we use a root-finding algorithm, Broyden's method [Bro65], which is similar to the popular Newton's method. In Broyden's method, the 16 partial derivatives entering in the 4×4 Jacobian matrix are replaced with finite differences. While the derivatives can be evaluated analytically from the CLD expressions with ease, using finite differences makes it easier to identify the effect of the different contributions entering in the WS cell energy. This point will be covered in greater detail in Chapter 3. The Jacobian matrix is not computed at each iteration but is only evaluated at the first iteration then simply rank-one updated. In order to avoid an unreliable estimation

of the equilibrium composition $\{A_{eq}, I_{eq}, n_{0,eq}, n_{p,eq}, n_{g,eq}\}$ due to the accumulation of errors, the maximum number of iterations is fixed to $N_{iter}^{max} = 1000$. In addition, the backstepping technique is employed to avoid nonphysical solutions, such as negative values for A or $|I| > 1$, that could result in errors when reinjected in the equilibrium equations. For instance, if at a given iteration, a spurious value of A is obtained, then we replace it by the previous value A_{old} plus a smaller step $\Delta A' < \Delta A$, until we get a physical value. Finally, let us mention that as for Newton's method, Broyden's method requires an initial guess for the composition.

We proceed as follows. The calculation starts at the neutron drip density n_{ND}. A natural choice for the initial guess is to take the last solution for the ground state of the outer crust, with reasonable values $A_{guess} = 36$, $I_{guess} = 0.3$, $n_{0,guess} = 0.15$ fm^{-3}, and $n_{g,guess} = 10^{-6}$ fm^{-3}. Then, the proton density is calculated as

$$n_{p,guess} = (n_B - n_{g,guess}) \left(1 - \frac{n_{g,guess}}{n_{0,guess}}\right) \frac{1 - I_{guess}}{2}. \tag{1.88}$$

To continue, we make use of Broyden's method described previously to evaluate the equilibrium composition A_{eq}, I_{eq}, $n_{0,eq}$, and $n_{g,eq}$. The process is then repeated with n_B increasing in steps of $\Delta n_B = 10^{-4}$ fm^{-3}. At each new value of n_B, the guess is updated to coincide with the last equilibrium composition, ensuring faster convergence of the algorithm. At a reasonable value of baryon density, $n_B = 10^{-3}$ fm^{-3}, we start to check whether it is beneficial or not to have a phase transition from clusterized matter to homogeneous matter. The calculation is stopped once the crust-core (CC) interface is reached, approximately for $n_B \approx n_{sat}/2$. The CC transition from the crust side is discussed in details in 1.2.6.

1.2.3.2 Equilibrium composition

Fig. 1.7 shows the evolution with baryon density n_B of the equilibrium composition of the inner crust. The empirical parameters entering in the bulk part of the CLDM energy correspond to the BSk24 effective force [GCP13], and the surface parameter p is fixed at the educated value $p = 3$, which appears to be a reasonable value for Skyrme-type functionals, as we will discuss in 1.2.6.

It is found that the number of nucleons inside the cluster A as well as inside the WS cell A_{WS} monotonously increases with increasing density, going up to ≈ 700 and ≈ 1500, respectively, at high density. The number of free neutrons $N_g = A_{WS} - A$ can also be inferred. It is obviously equal to zero at the neutron drip density, since $A = A_{WS}$. The behavior of A and A_{WS} is in agreement with other CLD calculations, such as the one of BBP [BBP71] and that of DH [DH00]. The later study reports a value of $A \approx 600$ at the CC interface, using the SLy4 functional, while BBP report a much higher value of $A = 7840$ (see their Table 1). Let us notice that the presence of such heavy spherical nuclei at the crust bottom raises the question of stability with respect to deformation and fission, as explained in [DH00]. In particular, nuclear fission, the approximate condition for which is $R_p/R_{WS} \gtrsim 1/2$ [BW39; PR95], R_p being the proton radius, could occur at high density. In 1.2.5, we show that considering nonspherical geometries can stabilize the large clusters. It is important to stress that the composition, in particular A and

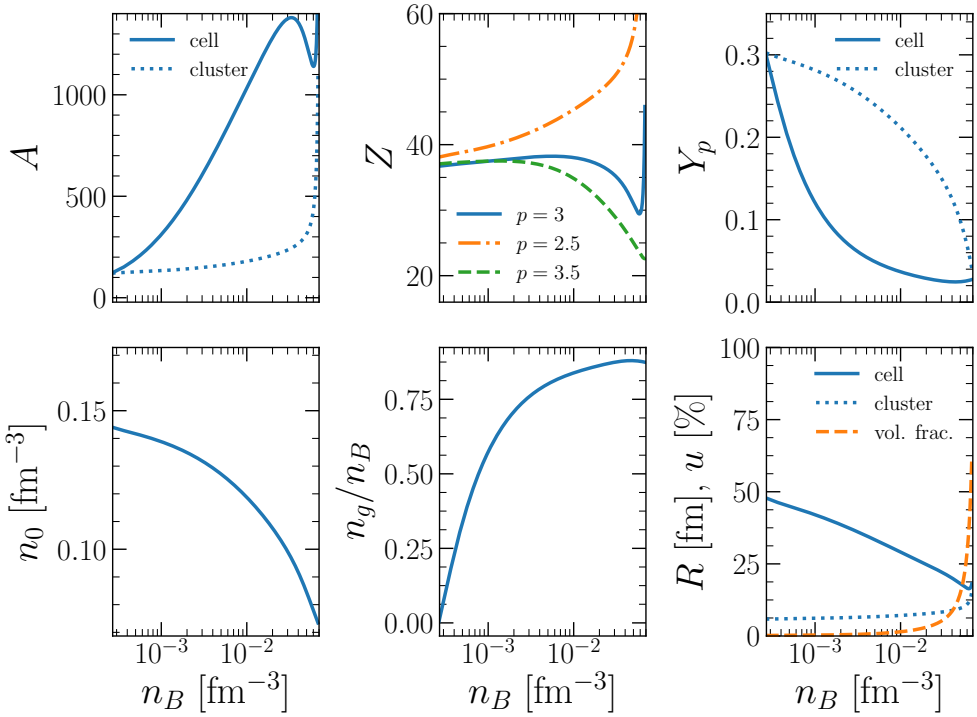

Figure 1.7: Variation with baryon density n_B of the equilibrium value of mass number A, atomic number Z, proton fraction Y_p, average cluster density n_0, neutron gas density to baryon density ratio n_g/n_B, radius R, and volume fraction u in the inner crust, for BSk24 CLDM with $p = 3$. Solid (dotted) lines correspond to the results for the cell (cluster). In the upper-mid panel, three values of the parameter p are selected: $p = 2.5$, $p = 3$, and $p = 3.5$.

Z, is very sensitive to the isospin dependence of the surface tension at extreme isospin ratios.

The variation with baryon density of the equilibrium value of Z is also represented in Fig. 1.7. We find $Z \approx 40$ all along the inner crust with $p = 3$, which is in a surprisingly good agreement with microscopic results. In particular, in the early work of Negele and Vautherin (NV) [NV73] is derived a set of nonlinear equations for the single particle wave functions of nucleons, using the density-matrix expansion for a realistic NN interaction. NV observed a predominance of $Z = 40$ at low density, and $Z = 50$ at high density. Subsequent works within the semiclassical ETF [Gor+05] and finite-temperature extended Thomas-Fermi plus Strutinsky integral (TETFSI) [Ons+08; Pea+18] also predict $Z = 40$ in the inner crust. As far as CLD calculations are concerned, DH find that the equilibrium value of Z is almost constant in the vicinity of ≈ 40 throughout the inner crust, whereas BBP find monotonically increasing values of Z. Once again, it should be stress out that Z is very sensitive to the isospin dependence of the surface tension. In particular, it is observed by varying the parameter p that governs the behavior of the surface

tension at extreme isospin values. We can see that a lower surface tension, $p = 3.5$, favors smaller atomic number Z, and in general lighter clusters, unlike $p = 2.5$ that leads to heavier clusters.

As in the outer crust, we find that the proton fraction inside the cell Y_p continuously decreases in the free neutron regime, dropping from ≈ 0.3 at the neutron drip point to ≈ 0.03 at the edge of the crust. With increasing density, clusters also becomes more and more asymmetric, I going up to ≈ 0.85 in the bottom layers.

Clusters are found to be more and more dilute with n_B increasing. At the neutron drip density, we get $n_0 \approx 0.145$ fm^{-3}, which is close to the saturation density of SNM of the BSk24 functional, $n_{sat} = 0.1578$ fm^{-3}. At the CC interface, the cluster density is as low as $n_0 \approx 0.07$ fm^{-3}, which is comparable to the neutron gas density, represented is the lower-mid panel. It is seen that the ratio n_g/n_B rapidly reaches $\approx 75\%$ at $n_B = 2 \times 10^{-3}$ fm^{-3} then stays approximately constant at higher densities.

The equilibrium radius of the spherical WS cell R_{WS} and of the spherical cluster R_{cl} are also displayed in Fig. 1.7. As DH, we observe that R_{WS} monotonically decreases unlike R_{cl} that slowly increases with increasing depth. Therefore, nuclei becomes closer and closer, eventually becoming close enough to touch each other at some point, creating a very large cluster, ultimately leading to homogeneous matter. We can also understand this by calculating the volume fraction $u = (R_{cl}/R_{WS})^3 = 2n_p/(n_0(1-I))$ (orange dashed line). We find that the cluster fills up to 60% of the WS cell volume at the CC interface. This feature combined with the virial theorem, Eq. (1.69), outlines the fact that lattice and finite-size contributions to the Coulomb energy are crucial for the determination of the ground state of the inner crust.

1.2.3.3 Equation of state

In Fig. 1.8, the equilibrium energy per nucleon of the WS cell $e_{WS} = E_{WS}/A_{WS}$ is plotted as a function of the baryon density n_B for different CLDM, based on the relativistic model DD-MEδ, and on three Skyrme-type interactions: SLy4, BSk22, and BSk24. It is observed that e_{WS} depends on the nuclear model. In particular, it is known to be correlated with the symmetry energy, with higher symmetry leading to higher e_{WS}, at subnuclear densities [Pea+18]. This trend can be verified by looking at the right panel of the figure, that shows the symmetry energy, Eq. (1.52), as a function of density for the four models considered here.

Fig. 1.8 also shows the variation with the baryon density of pressure P, commonly referred to as the EoS, in the inner crust. We demonstrate in Appendix C that the total pressure, defined by the first law of thermodynamics as

$$P = n_B^2 \frac{de_{WS}}{dn_B}, \tag{1.89}$$

can be expressed as

$$P = P_g + P_e + P_L, \tag{1.90}$$

at the equilibrium composition, where P_L is the lattice contribution to the total pressure. Using this expression rather than finite differences to estimate the derivative, Eq. (1.89), is more reliable and has the advantage to be faster from the computational point of view.

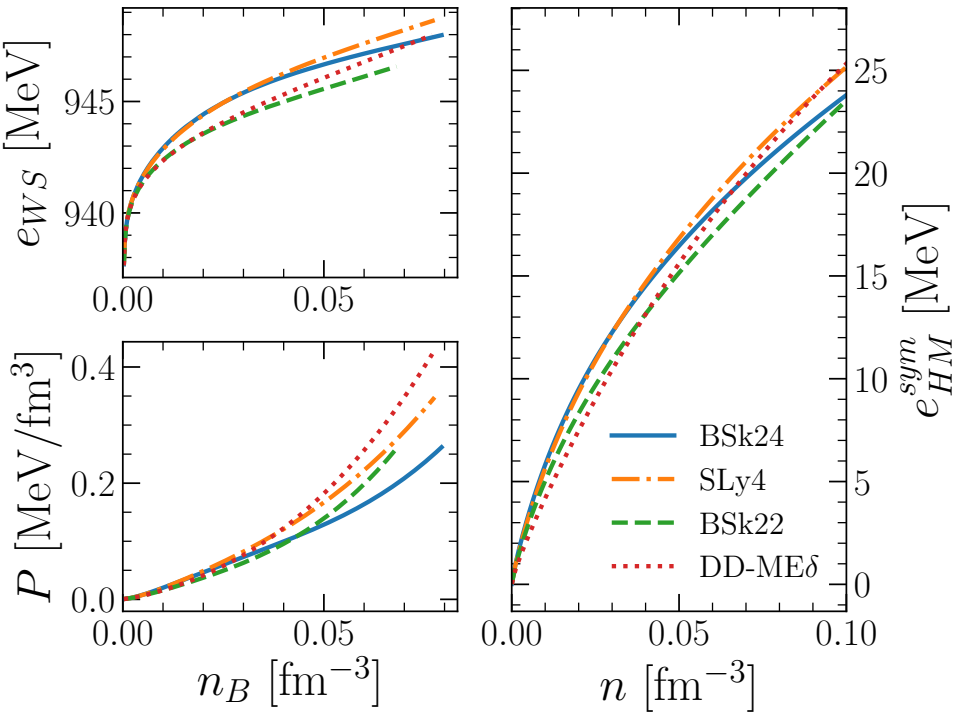

Figure 1.8: Left: Equilibrium value of the energy per nucleon of the WS cell $e_{WS} = E_{WS}/A_{WS}$ (upper panel), and pressure P (lower panel) as a function of the baryon density n_B in the inner crust for four selected CLDM: BSk24, SLy4, BSk26, and DD-MEδ. Right: Variation of symmetry energy e_{HM}^{sym}, Eq. (1.52), with density n, for the four models.

In addition, it allows identifying the different contributions to the pressure. In the inner crust, the pressure is no longer dominated by the relativistic electron gas but by the ambient neutron gas [Car17b]. At subnuclear densities, we observe that the EoS is also correlated with the symmetry energy. In particular, the higher the empirical parameter E_{sym}, which is the symmetry energy at $n = n_{sat}$, the stiffer is the EoS. The value of E_{sym} for each model is reported in Table 1.3.

1.2.4 Strutinsky shell corrections to the CLD energy

In the CLD approximation, shell effects, which are known since the pioneering work of BPS [BPS71] to be essential to correctly evaluate the outer-crust composition at zero temperature, are lost. In this same limit microscopic calculations have shown that the neutron shell effects become vanishingly small beyond the neutron drip point [Cha06; Cha+07], but proton shell effects persist in the inner crust.

There are different ways to include shell corrections to the CLD energy. The simplest approach is to use an empirical formula, such as the one proposed by Myers and Swiatecki [MS66] which is accurate for reproducing masses of laboratory nuclei. However, a

limitation of their method is that it requires a priori a list of magic numbers, which are obviously not known in the regime of the inner crust. Let us recall that NV find a persistence of $Z = 40$ while it is not considered as a magic number in ordinary nuclei. A more suitable alternative is to calculate shell corrections using the Strutinsky method [Ons+08]. Fortunately, Strutinsky shell corrections were calculated for modern BSk functionals, and are tabulated in [Pea+18] (see Supplementary data). We therefore add these corrections on top of the CLD energy for the corresponding models.

We now turn to the numerical method, proceeding as follows. The energy density is the quantity to be minimized at constant baryon density for a fixed number of protons inside the WS cell. We derive the system of equilibrium equations using the Lagrange multipliers method, as in 1.2.2, yielding

$$\frac{\partial E_{cl}}{\partial A} - \frac{E_{cl}}{A} = \frac{1-I}{2}\left(\mu_e(n_p) + \frac{2np}{A(1-I)}\frac{\partial E_{cl}}{\partial n_p} - \frac{2}{A}\frac{\partial E_{cl}}{\partial I} + \Delta m_{pn}c^2\right), \tag{1.91}$$

$$\frac{\partial E_{cl}}{\partial A} + \frac{1-I}{A}\frac{\partial E_{cl}}{\partial I} + \frac{P_g(n_g)}{n_0} = \mu_g(n_g) - m_n c^2, \tag{1.92}$$

$$\frac{n_0^2}{A}\frac{\partial E_{cl}}{\partial n_0} = P_g(n_g). \tag{1.93}$$

Let us notice that beta equilibrium is not imposed anymore since Z is fixed, causing a modification of Eq. (1.91) with respect to the virial theorem with curvature term, Eq. (1.84). For a given n_B, the minimization is carried out for each tabulated Z using Broyden's method. The proton Strutinsky shell corrections are then added perturbatively to the CLD energy by interpolation among values of the table, which gives the shell energy per nucleon for a given (n_B, Z). The WS energy density including shell corrections thus reads

$$\varepsilon_{WS}(n_B, Z) = \varepsilon_{WS}^{CLD}(n_B, Z) + n_B \Delta e_{sh}(n_B, Z), \tag{1.94}$$

where ε_{WS}^{CLD} is the smooth part of the WS energy density at the equilibrium, and Δe_{sh} is the interpolated shell energy per nucleon. The value of Z that minimizes the energy density of matter is naturally defined as the equilibrium value.

Fig. 1.9 shows the variation of the WS energy density as a function of Z at two selected values of baryon density n_B, for BSk24 CLDM. As expected, the pure CLD results, represented in dotted lines, are close to those including Strutinsky shell corrections, represented in solid lines, for closed-shell configurations, while remarkable differences exist for all other values of Z. This feature confirms the importance of a proper account of the shell structure. At $n_B = 10^{-3}$ fm^{-3}, a competition between $Z = 40$ and $Z = 50$ can be observed, with $Z = 40$ being slightly favored. However, it should be stressed that the difference in energy density is about 10^{-6} MeV/fm^{-3}, which is expected to be lower than the precision reached by our modeling. It is observed that the shell closure $Z = 40$ is also favored over $Z = 50$ and $Z = 58$ at $n_B = 10^{-2}$ fm^{-3}.

Our results for the equilibrium value of Z in the inner crust using BSk22, BSk24, BSk25, and BSk26 CLDM with (solid lines) and without (dotted lines) Strutinsky shell corrections can be seen in Fig. 1.10. It can be observed that magic numbers are recovered

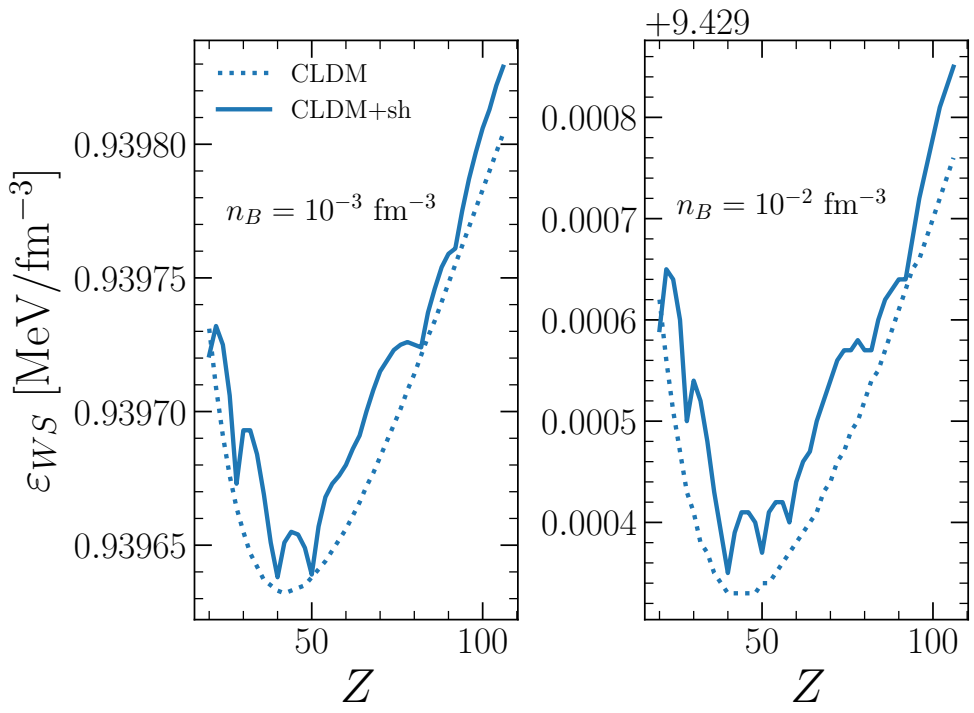

Figure 1.9: WS cell energy density as a function of number of protons Z at two different densities in the inner crust for BSk24 CLDM with (solid lines) and without (dotted lines) Strutinsky shell corrections on top of the CLD energy. In the right panel, the constant value 9.429 MeV/fm^3 is subtracted from the WS cell energy density.

when shell corrections are added on top of the CLD energy. In particular, remarkable stability at $Z = 40$ is seen for BSk24 and BSk26, as well as $Z = 20$ and $Z = 40$ for BSk22, in a very good agreement with Fig. 12 of [Pea+18]. A small difference only appears for the BSk25 model, reflecting the limitations of the CLD approach. For this functional, after the plateau at $Z = 50$, also obtained with extended Thomas-Fermi plus Strutinsky integral (ETFSI) calculations of [Pea+18] for the same functional, the equilibrium number of protons drops to $Z = 40$ in our case, instead of increasing as in [Pea+18]. However, we stress that the authors find a second minimum at $Z = 40$, and the energy difference between the two minima is of the order of 10^{-3} MeV [Pea+19].

Let us recall that surface and curvature parameters σ_0, b_s, σ_{0c}, and β are so far fitted to experimental masses of nearly symmetric nuclei from the AME2016 [Hua+17] with a fixed value of the parameter p that governs the behavior of the surface tension at extreme isospin values. Therefore the shell energy is implicitly accounted for in the surface tension by underestimating the value of σ_0, that is the surface tension of symmetric nuclei. This results in predicting slightly overbound nuclei with the CLD approach, but overall in a better description of spherical nuclei. However, we face an issue when adding Strutinsky shell corrections to the CLD energy, since we do not want to

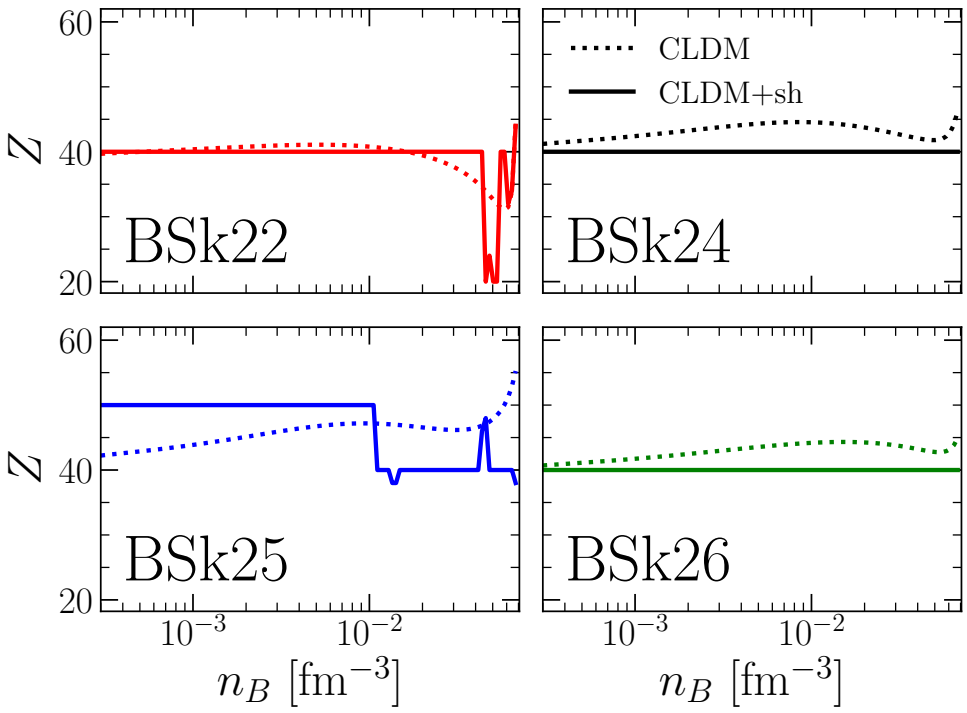

Figure 1.10: Equilibrium value of Z as a function of baryon density n_B in the inner crust for BSk22, BSk24, BSk25, and BSk26 CLDM with (solid lines) and without (dotted lines) Strutinsky shell corrections on top of the CLD energy.

double-count the shell energy. To address this problem, we fit the surface and curvature parameters to the ETF results for each functional [Pea19], keeping the parameter p fixed to the value $p = 3$ [Car+19], which gives an accurate reproduction of the CC transition points obtained in [Pea+19].

1.2.5 Nonspherical pasta phases

We have assumed so far that the inner crust only consists of spherical clusters. However, at high density just before the CC transition, nuclei are almost close enough to touch each other, and thus the lattice energy significantly reduces the Coulomb energy. Consequently, matter could in principle arrange itself into exotic structures, sometimes referred to as nuclear "pasta". In particular, from the density at which the volume fraction exceeds 1/2, it is expected that nuclei turn inside out, therefore forming neutron bubbles immersed in a proton-rich phase (the former cluster) [BBP71]. Furthermore, molecular dynamics simulations, in which a large number of interacting nucleons are let evolving in a very large box, predict the appearance of complex structures for $Y_p \approx 0.1$, which is comparable to the typical value in the bottom layers of the inner crust of neutron stars [Wat+03]. It should be stressed that these exotic phases of matter could

constitute half of the crust mass [LRP93]. It is therefore straightforward to imagine that various astrophysical phenomena, such as the cooling process by neutrino emission, can be affected by their existence [WM11].

One of the virtue of the CLD approach is that different geometries for nuclear clusters can be considered in a simple way, allowing for the study of the pasta phases [RPL83; LS91; LRP93; NGL12]. Let us first recall the virial theorem with curvature term, here expressed in term of the surface, curvature, and Coulomb energy densities,

$$\varepsilon_{surf} + 2\varepsilon_{curv} = 2\varepsilon_{Coul}. \tag{1.95}$$

Following [RPL83; NGL12], the general expression for the surface energy density is

$$\varepsilon_{surf} = \frac{ud\sigma}{r}, \tag{1.96}$$

and that of the curvature energy density is

$$\varepsilon_{curv} = \frac{ud(d-1)\sigma_c}{r^2}, \tag{1.97}$$

where the surface tension σ and curvature tension σ_c are independent of the dimensionality, and therefore given by Eqs. (1.59) and (1.61), respectively. The Coulomb energy density reads

$$\varepsilon_{Coul} = 2\pi(eY_p n_0 r)^2 u \eta_{Coul,d}(u), \tag{1.98}$$

with $\eta_{Coul,2} = \frac{1}{4}\left[\ln\left(\frac{1}{u}\right) + u - 1\right]$ for $d = 2$, and $\eta_{Coul,d}(u) = \frac{1}{d+2}\left[\frac{2}{d-2}\left(1 - \frac{du^{1-2/d}}{2}\right) + u\right]$ otherwise.

In the previous expressions, r represents the radius (half-width in the case of planar geometry) of clusters or holes, u the volume fraction occupied by the cluster (hole), n_0 the density of the dense phase, and Y_p its associated proton fraction. The expression of the volume fraction is different depending on whether we have clusters or holes:

$$u = \begin{cases} (n_B - n_g)/(n_0 - n_g) & \text{for clusters,} \\ (n_0 - n_B)/(n_0 - n_g) & \text{for holes.} \end{cases} \tag{1.99}$$

The parameter $d = \{3, 2, 1\}$ is related to the dimensionality, with $d = 3$ for spheres and bubbles, $d = 2$ for cylinders and tubes, and $d = 1$ for plates. In the former case, we naturally recover the expressions Eqs. (1.58), (1.60), and (1.56). Also, let us note that nuclei and bubble phases are identical as far as plates are concerned.

Replacing these quantities in Eq. (1.95), we obtain an equation for the cluster (hole) radius/half-width,

$$4\pi(eY_p n_0)^2 \eta_{Coul,d}(u) r^4 - d\sigma r - 2d(d-1)\sigma_c = 0, \tag{1.100}$$

which has to be solved numerically. Let us notice that, neglecting the curvature term, the virial theorem reduces to $\varepsilon_{surf} = 2\varepsilon_{Coul}$, thus the expression of the r is analytical,

$$r = \left(\frac{d\sigma}{4\pi(eY_p n_0)^2 \eta_{Coul,d}(u)}\right)^{1/3}. \tag{1.101}$$

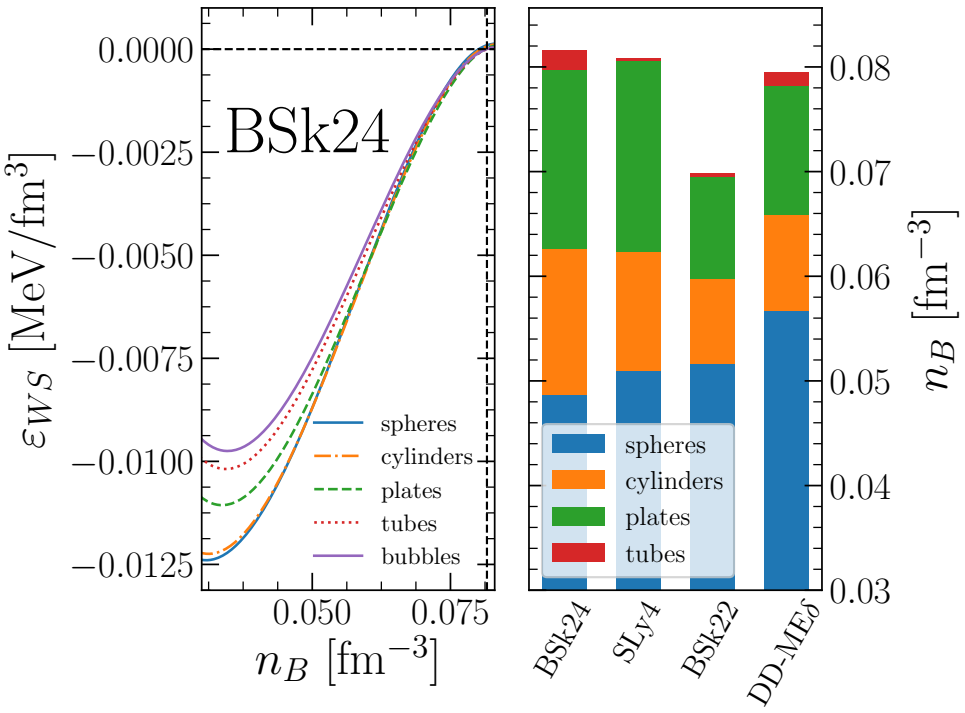

Figure 1.11: Left panel: energy density of matter as a function of baryon density for the five phases, using BSk24 CLDM. The black dashed lines mark the CC transition point. Right panel: equilibrium phase as a function of baryon density for four selected CLDM: BSk24, SLy4, BSk22, and DD-MEδ. For these calculations, the surface parameter p is fixed to the value $p = 3$.

In order to find the most stable phase at a given baryon density, we proceed as follows. The composition is first calculated at a given n_B in the spherical nuclei case ($d = 3$) following 1.2.2. Then, keeping the same composition, the radius/half-width r is evaluated for the five different phases by solving numerically Eq. (1.100). Finally, since the bulk and electron contributions to the WS cell are independent of the dimensionality, the equilibrium phase is the one that minimizes $\varepsilon_{surf} + \varepsilon_{curv} + \varepsilon_{Coul}$. Let us notice that this method has to be considered as an approximation since we do not consider the dimensionality dependence of the surface plus curvature energy in the minimization. This is similar to the so-called "coexisting phase method" employed in several works [Ava+08; Ava+10; Gra+17].

In the left panel of Fig. 1.11, we represent the WS energy density as a function of the baryon density for the five phases, using our CLDM to calculate the surface and curvature energy for the BSk24 functional. It is clearly seen that the spheres dominates up to $n_B \approx 0.05$ fm^{-3}, which is in good agreement with the semiclassical ETF results for this force [PCP20]. From this density, we find cylinders up to $n_B \approx 0.065$ fm^{-3}, before observing a transition to plates. Then, the differences in energy density become so

small that the possible transition to another phase cannot be distinguished in the figure. However, one could expect the usual sequence, that is a transition to tubes eventually followed by one to bubbles before the final transition to homogeneous matter [RPL83], here marked by the black dashed lines.

The right panel of Fig. 1.11 shows the equilibrium phase as a function of n_B for four CLDM: BSk24, SLy4, BSk22, and DD-MEδ. While model dependence is observed, it is interesting to notice that the sequence spheres $\rightarrow$ cylinders $\rightarrow$ plates $\rightarrow$ tubes is recovered for every model. Another shared feature is that the transition to homogeneous matter is found before the appearance of bubbles. Let us remark that pasta phases are observed for SLy4 here, while previous CLD and TF calculations for this functional have predicted that the sphere is the most favorable shape at all densities up to the CC transition point [DH00; Viñ+17]. This contradiction can be understood by the fact that we are dealing with very tiny differences in energy density (all the shapes are very close), in a region where the matter is extremely neutron rich, thus where the nuclear surface tension is poorly constrained. In particular, we observed that varying the value of the surface parameter p can affect the sequence of pasta phases.

1.2.6 Crust-core transition from the crust side

It is well known that a phase transition from a solid crust to a liquid core takes place at some ≈ 1 km from the surface of the star, corresponding to subsaturation densities. A precise estimation of this transition point is necessary in order to evaluate the crust mass, thickness and moment of inertia, and so to understand phenomena involving NS, such as glitches, that are irregularities in the their rotational motion [Esp+11]. In that sense, a Bayesian analysis of the CC transition has been performed [CGM19] and is presented in details in Chapter 2.

The simplest approach for computing the phase transition is from the core side, in which the transition is defined as the density point where homogeneous nuclear matter (NM) at beta equilibrium becomes unstable with respect to density fluctuations. Two versions of this technique can be distinguished: the so-called thermodynamical [Gon+17] and dynamical [PRL95; Ant+19] methods.

The former method consists in evaluating the thermodynamical spinodal, that is the instability point of NM with respect to the liquid-gas (LG) phase transition. The only necessary nuclear physics input for this method is the energy functional of homogeneous NM, which can is well constrained through nuclear experiments and/or ab initio calculations in the vicinity of the nuclear saturation density n_{sat}. While it appears as a substantial advantage, it is known that the dynamics of the CC transition is very different from the LG one [DCG07; Duc+07; DMC08], thus applying this method results in an overestimation of the CC transition density and pressure. Indeed, the CC transition is expected to take place at approximately $\approx n_{sat}/2$, where the energy density of clusterized matter overcomes that of uniform NM [BBP71]. Since Coulomb, surface, and curvature terms, that are crucial for determining the equilibrium composition in the inner crust, vanish in homogeneous NM, they no not contribute to the determination of the LG thermodynamical spinodal.

In the dynamical method, finite-size density fluctuations are added, thus it is expected

to give a better estimation of the CC transition and pressure. It should be stressed that the isovector gradient terms, which are needed in addition to the EoS with respect to the thermodynamical method, play a nonnegligible role for the determination of the dynamical spinodal, the location of which also depends on the many-body formalism adopted [DMC08].

While the dynamical method gives a better estimation of the CC transition point in comparison with the thermodynamical one, one should remark that the spinodal decomposition scenario is not compatible with the equilibrated crust in which matter is not uniform but composed of clusters immersed in a sea of electrons and neutrons. For this reason, the CC transition point is here computed from the crust side, by comparing the energy density of the two competing phases in beta equilibrium. The equation for the CC transition density n_t is thus

$$\varepsilon_{WS}^{crust}(n_t) = \varepsilon_{npe}(n_t), \tag{1.102}$$

where ε_{WS}^{crust} is the equilibrium energy density in the WS cell in the inner crust, and ε_{npe} is the equilibrium energy density of matter in the outer core, which consists of homogeneous *npe* matter, studied in Section 1.3. The CC transition point is computed in the following for several nuclear models, using the metamodeling technique extended to finite nuclei in the CLD approximation, Eq. (1.62), to calculate the WS cell energy density in the inner crust, and keeping the same empirical matter for the description of uniform *npe* matter. One should stress the importance of having a unified EoS for the crust and the core [DH01] to estimate correctly the CC transition point. Indeed, it was shown that matching a crust and core EoS based on different nuclear models induce an uncertainty on the determination of the CC transition point, consequently inducing an uncertainty in the crustal observables, which can be as large as 30% for the crust thickness [For+16].
Let us mention that pasta phases are not considered here, since we have checked that their presence does not affect the estimation of the CC transition density and pressure.

In Fig. 1.12, we show the variation with surface parameter p of n_t for SLy4 CLDM. For each value of p, the surface and curvature parameters are fitted to experimental masses from the AME2016. The CC transition density is estimated for different values of the truncation order N in the density development, Eq. (1.50). A convergence feature is observed from $N = 2$ to $N = 4$, almost achieved at $N = 3$. We can see that truncating at $N = 2$ leads to a substantial underestimation of about $\approx 20\%$ of the transition density. This observation highlights the importance of keeping high-order parameters beyond (Q_{sat}, Q_{sym}) $(N = 3)$, and (Z_{sat}, Z_{sym}) $(N = 4)$ in the Taylor expansion.
A strong correlation is seen between the isovector surface parameter p and n_t: the higher the value of p the higher the transition density. This can be understood from the fact that a low value of p leads to a higher surface tension at extreme isospin values, thus it makes the cluster less bound and consequently the uniform *npe* matter becomes the favorable phase at lower density.
Different estimations of the CC transition density for the SLy4 functional found in the literature are reported in Fig. 1.12 (black lines), with n_t ranging from 0.072 fm^{-3} [Viñ+17], in the CLD approximation, to 0.089 fm^{-3} [Duc+11] (not represented in the figure), with the thermodynamical method. It is interesting to observe that the two

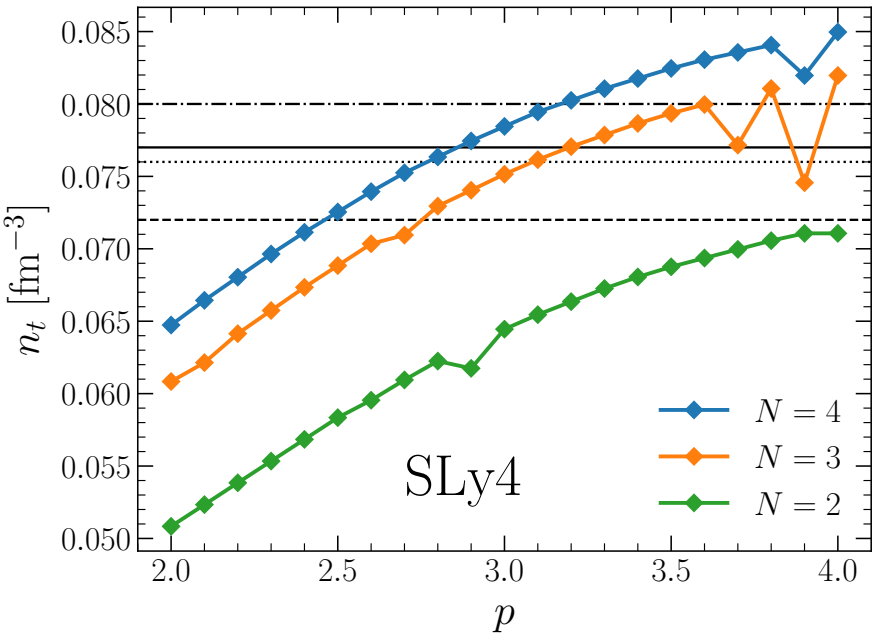

Figure 1.12: Crust-core transition density as a function of the surface parameter p with truncation order $N = 2$, $N = 3$, and $N = 4$, for SLy4 CLDM. The black horizontal bars represent different evaluations of n_t for the SLy4 functional found in the literature: $n_t = 0.072$ fm^{-3} [Viñ+17] (dashed line) and $n_t = 0.077$ fm^{-3} [DH00] (solid line) in the CLDM approximation, $n_t = 0.076$ fm^{-3} [Viñ+17] (dotted line) in the TF approximation, and $n_t = 0.080$ fm^{-3} [Viñ+17] (dashdotted line) with the dynamical method.

different CLDM calculations of the literature based on SLy4 functional, reported in the figure, give a different estimation of n_t, with 0.072 fm^{-3} in [Viñ+17], and 0.077 fm^{-3} in [DH00]. This stresses once again the importance of the treatment of the isovector surface tension for the determination of the CC transition point.
The effect of the varying the low-density parameter b on n_t is also evaluated in [CGM19]. It is found that while it does not significantly affect the transition density in comparison with N and p, it should be kept as an additional EoS parameter in any statistical analysis in order to make a quantitative prediction of the CC transition point. The introduction of the parameter b in the parameter space is, in fact, an effective manner to account for the effect of orders $N > 4$, which is not important.

Fig. 1.13 shows our estimations of the transition density n_t and pressure P_t as a function of the slope of the symmetry energy L_{sym} for a set of relativistic and nonrelativistic functionals, in comparison with the dynamical spinodal calculations of [Duc+11]. It is seen that the value $p = 3$ is in good agreement with the dynamical results for most of the models. For DD-ME2, the lower value needed for p is supported by the TF calculations in [GPA12].
As in [Viñ+17], an anticorrelation is observed between L_{sym} and n_t. Using a linear re-

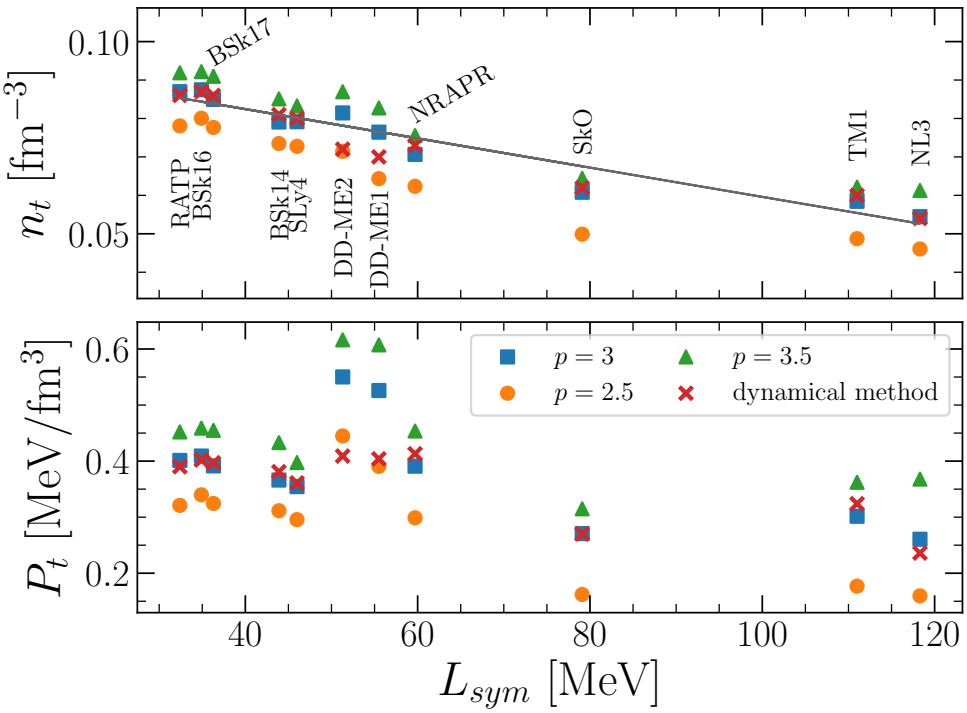

Figure 1.13: Crust-core transition density n_t (upper panel) and pressure P_t (lower panel) as a function of L_{sym} for several interactions. The crosses are the transition points calculated in [Duc+11] using the dynamical spinodal. The circles, squares, and triangles correspond respectively to our estimation of the transition points with $p = 2.5$, $p = 3$, and $p = 3.5$. The gray line is the linear regression curve fitted to the $p = 3$ results.

gression to model the relationship between L_{sym} and our estimation of n_t with $p = 3$, we find $n_t = -3.807 \times 10^{-4} L_{sym} + 0.098$ fm^{-3}, for a root mean square error of 3.094×10^{-3} fm^{-3}. This is linear equation for n_t is in very good agreement with Eq. (17) of [Duc+11]. This downwards tendency with increasing values of L_{sym} is not clearly observed for the transition pressure. We will see in Chapter 2 that the relation between those two quantities is less explicit because P_t rather depends on K_{sym}, which is logical because the pressure requires the calculation of one more derivative in comparison to the energy density that defines n_t.

1.3 Matter of the core

In the very bottom layers of the inner crust, clusters are so large and asymmetric that the CLD energy per nucleon, Eq. (1.62), becomes equal to that of infinite nuclear matter, marking the CC interface. While the composition and structure of the core close to the saturation density are well known, various scenarios have been proposed in the literature [Oer+17] concerning the relevant degrees of freedom above $2 - 3n_{sat}$.

This section deals with the matter of the core. In 1.3.1 we derive the system of variational equations for the ground state of the outer core. The model dependence of the composition and EoS is then explored. In particular, we focus on apparent correlations with the symmetry energy. The matter inside the inner core is finally discussed in 1.3.2.

1.3.1 Outer core: homogeneous *npeμ* matter

From the CC transition point, previously discussed in 1.2.6, up to $n_B \approx 2n_{sat}$, the matter of the core consists of a uniform plasma of neutrons, protons, electrons, and eventually muons, hereafter referred to as *npeμ* matter (or *npe* if muons are not present). This region of the star corresponds to the outer core. The energy density of *npeμ* matter reads

$$\varepsilon_{npe\mu}(n_B,\delta,n_e,n_\mu) = \varepsilon_{HM}(n_B,\delta)+\varepsilon_e(n_e)+\varepsilon_\mu(n_\mu)+n_B\frac{1-\delta}{2}\Delta m_{pn}c^2+n_B m_n c^2, \quad (1.103)$$

with $\varepsilon_{HM} = ne_{HM}$ the energy density of nuclear matter given by the metamodel, Eq. (1.37). The expression of energy density of the relativistic muon gas $\varepsilon_\mu(n_\mu)$ is the same as that of the relativistic electron gas, and it is derived in Appendix A.

1.3.1.1 Variational equations

Following 1.2.2, the system of differential equations determining the equilibrium composition and EoS in the outer core is determined by minimizing the energy density of matter, Eq. (1.103), at constant baryon density under the condition of overall charge neutrality, which now reads

$$n_B\frac{1-\delta}{2} = n_e + n_\mu. \quad (1.104)$$

since muons may exist in this region of the star. Muons are present in the outer core if the electron chemical potential exceeds the muon rest-mass energy, that is $\mu_e \gtrsim m_\mu c^2$. As far as variational variables are concerned, a reasonable choice appears to be the asymmetry δ and the muon density n_μ. Let us first minimize the energy density of matter with respect to δ,

$$\begin{aligned} \left.\frac{\partial\varepsilon_{npe\mu}}{\partial\delta}\right|_{n_\mu} &= 0 \\ 2\frac{\partial e_{HM}}{\partial\delta} - \Delta m_{pn}c^2 - \mu_e &= 0. \end{aligned} \quad (1.105)$$

We can easily identify this equation with the well-known beta equilibrium condition. Indeed, using the definition of the neutron and proton chemical potentials, Eq. (1.53), we obtain

$$\mu_n = \mu_p + \mu_e. \quad (1.106)$$

We now turn to minimization with respect to the muon density,

$$\begin{aligned} \left.\frac{\partial\varepsilon_{npe\mu}}{\partial n_\mu}\right|_{\delta} &= 0 \\ \mu_\mu - \mu_e &= 0, \end{aligned} \quad (1.107)$$

where we have introduced the muon chemical potential $\mu_\mu = \partial\varepsilon_\mu/\partial n_\mu$. This equation corresponds to the chemical equilibrium between muons and electrons, and has to be satisfied if muons are present. These two equations, Eq. (1.106) and (1.107), express the equilibrium with respect to the weak interaction processes. Let us remark that each time we mention electrons and muons, we are always referring to their net number, that is particles minus antiparticles.

From the numerical point of view, we use Broyden's method to solve the beta equilibrium equation, Eq. (1.106), starting from the transition density n_t. The initial guess for the asymmetry δ_{guess} is taken to be the value of the global asymmetry inside the WS cell at the CC transition point, which is approximately ≈ 0.9. At each new step of baryon density, the value of δ_{guess} is updated with the last equilibrium solution, and we check if $\mu_e \gtrsim m_\mu c^2$. In the case of $npe\mu$ being energetically favorable, Eq. (1.107) is added as a supplementary equation to be solved, setting the initial guess for the muon density to $n_{\mu,guess} = 10^{-5}$ fm^{-3}. The calculation is stopped when the baryon density reach $\approx 2n_{sat}$, from which the composition of matter becomes less certain.

1.3.1.2 Equilibrium composition and equation of state

In Fig. 1.14, the proton fraction $Y_p = (1-\delta)/2$ and muon fraction $Y_\mu = n_\mu/n_B$ are plotted as a function of the baryon density for the four nuclear models BSk24, SLy4, BSk22, and DD-MEδ, the empirical parameters of which are listed in Table 1.3. The variation n_B of the electron fraction Y_e can be deduced from the charge neutrality condition, Eq. (1.104). Surprisingly, it is observed that the proton fraction rises with n_B in the outer core, while it monotonously decreases in the crust. A strong correlation between the proton fraction and the symmetry energy, represented in the right panel for the four models, is seen. One can relate the two quantities using the beta equilibrium condition. Indeed, we can easily go through Eq. (1.106) assuming a quadratic expansion for the NM energy per nucleon,

$$e_{HM}(n_B, \delta) \simeq e_{HM}(n_B, \delta = 0) + \delta^2 e_{HM}^{sym}(n_B). \tag{1.108}$$

In that case, the beta equilibrium condition reads

$$4\delta e_{HM}^{sym}(n_B) - \Delta m_{pn} c^2 = \mu_e(n_e), \tag{1.109}$$

and we can thus express the proton equilibrium proton fraction as a function of the symmetry energy,

$$Y_p = \frac{1}{2} - \frac{\mu_e(n_e) + \Delta m_{pn} c^2}{8 e_{HM}^{sym}(n_B)}. \tag{1.110}$$

From this equation it is clear that the higher the symmetry energy, the higher the proton fraction, which is the trend observed in the figure.
The density from which muons are present is also shown in the upper left panel. It appears that we are dealing with npe matter up to $n_B \approx 0.12$ fm^{-3}, and it is seen that the threshold density for the appearance of muons, when $\mu_e \gtrsim m_\mu c^2$, is not very sensitive to the nuclear model.

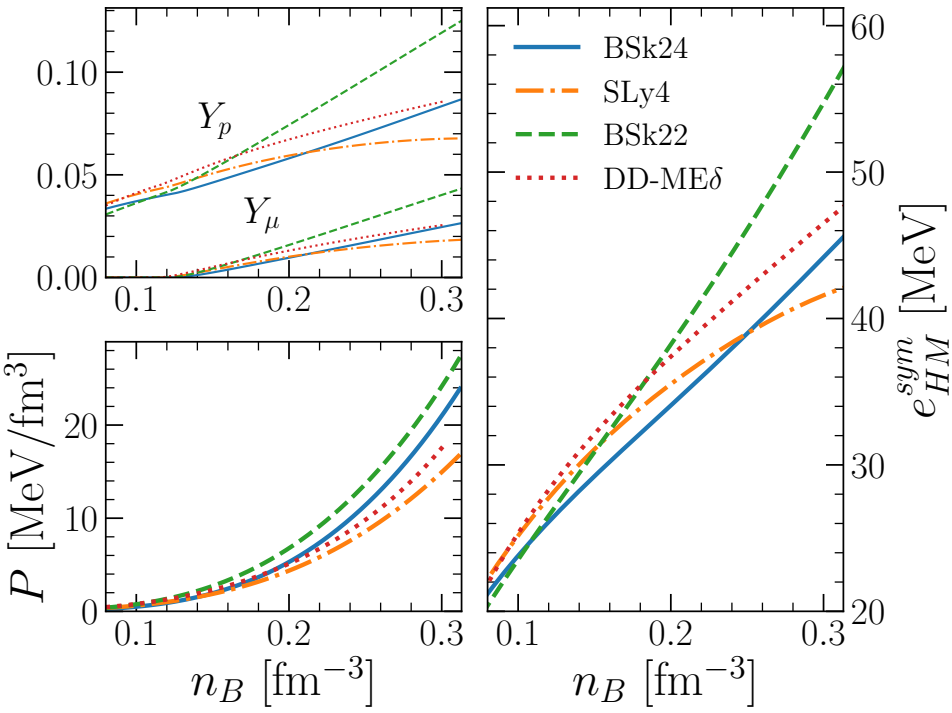

Figure 1.14: Left: Proton fraction Y_p and muon fraction Y_μ (upper panel), and pressure P (lower panel) as a function of the baryon density n_B in the outer core for four selected models: BSk24, SLy4, BSk22, and DD-MEδ. Right: Variation with baryon density of the symmetry energy e^{sym}_{HM}, Eq. (1.52), for the four models.

Fig. 1.14 also shows the pressure as a function of the density (lower left panel). In the outer core, we can write the pressure as

$$P(n_B) = P_{HM}(n_B, \delta) + P_e(n_e) + P_\mu(n_\mu), \tag{1.111}$$

where δ, n_e, and n_μ are the equilibrium values at n_B. The expression of the nuclear contribution P_{HM} is given by Eq. (1.54). The electron and muon contributions to the total pressure, respectively P_e and P_μ, share the same expression, Eq. (1.11), which is that of a relativistic Fermi gas. A strong model dependence is observed for the pressure at suprasaturation densities, reflecting the large uncertainties associated to the isovector parameters beyond E_{sym}, as reported in the last column of Table 1.3.

1.3.2 Inner core

From the crust-core interface up to $n_B \approx 2n_{sat}$, it is commonly accepted that matter is exclusively composed of neutrons, protons, electrons, and muons. At higher densities however, the composition of matter becomes uncertain and different scenarios have been considered in the literature for the structure and composition of the inner core [Oer+17].

The presence of hyperons at suprasaturation densities has been considered in many studies, and its effect on the EoS and subsequently on NS observables has been evaluated [Bed+12; For+15]. In particular, the presence of hyperons softens the high-density EoS and thus lowers the maximum mass of neutron stars. As a consequence, many models fail to satisfy the NS mass constraint of $2M_\odot$ [Ant+13], leading to the so-called "hyperon puzzle" [ZH13]. In fact, this measurement of a $2M_\odot$ NS also rules out most of the models that include a phase transition to quark matter or a boson condensate in the inner core, because the EoS is softened by the introduction of any additional degree of freedom without an interaction. Let us however mention a recently proposed EoS with a quark-hadron crossover at high density that allows a maximum mass of $2.35M_\odot$ [Bay+19] and agrees with the constraints on NS properties inferred from the GW170817 event [Abb+18; Abb+19].

We propose here to extrapolate the $npe\mu$ matter at higher densities, in the inner core. The different studies that consider hyperons and satisfy the maximum mass constraint show that the hyperon-nucleon and hyperon-hyperon are such that, if hyperons exist, they are not abundant and can be neglected as a first approximation, at least in the EoS energetics (see [Oer+17] and references therein). Since the metamodeling does not make any assumption regarding the degrees of freedom, but that the functional is based on a Taylor expansion, we can assume that the technique can be safely extended at high density in the aim of calculating static properties, such as the EoS or the mass-radius relation. The only thing that could invalidate it would be the presence of a large first-order phase transition, that is a large discontinuity in the EoS. Thus, the only hypothesis that is made here is considering that there is no such transition. Actually, even a transition to quark matter could be smooth. Indeed, several works consider pasta phases in the hadron-quark phase transition, with the effect of washing out discontinuities [MTC09; YMT09; YMT11; Yas+14]. Finally, this is equivalent to a null hypothesis: since the metamodeling allows to control uncertainties, a disagreement with astrophysical observations would be the sign of new physics, indicating either the existence of a first-order phase transition or an alternative theory of gravity. Let us recall that the metamodeling technique gives an accurate reproduction of existing nuclear models up to $\approx 2-3n_{sat}$ (metamodeling ELFc in [MHG18a]), as we have verified in Fig. 1.4. A solution for achieving faster convergence at high density, the metamodeling ELFd, is proposed in [MHG18a]. It is based on a reevaluation of the high-order empirical parameters parameters Q_{sat}, Q_{sym}, and Z_{sat}, Z_{sym}, by imposing a high-density point at which the energy per nucleon and the pressure are known for a given functional. This is encouraged by the fact that the impact of these parameters is very small in the vicinity of the saturation density. We will use this technique when we will want to reproduce existing hadronic models.

1.4 Unified metamodeling of the equation of state

As previously discussed, matching a crust and core based on different nuclear models can lead to large uncertainties associated with the CC transition density and pressure, which are the quantities for the determination of the crust observables. In particular, it was shown in [For+16] that it can lead to an error as large as $\approx 30\%$ for the crust

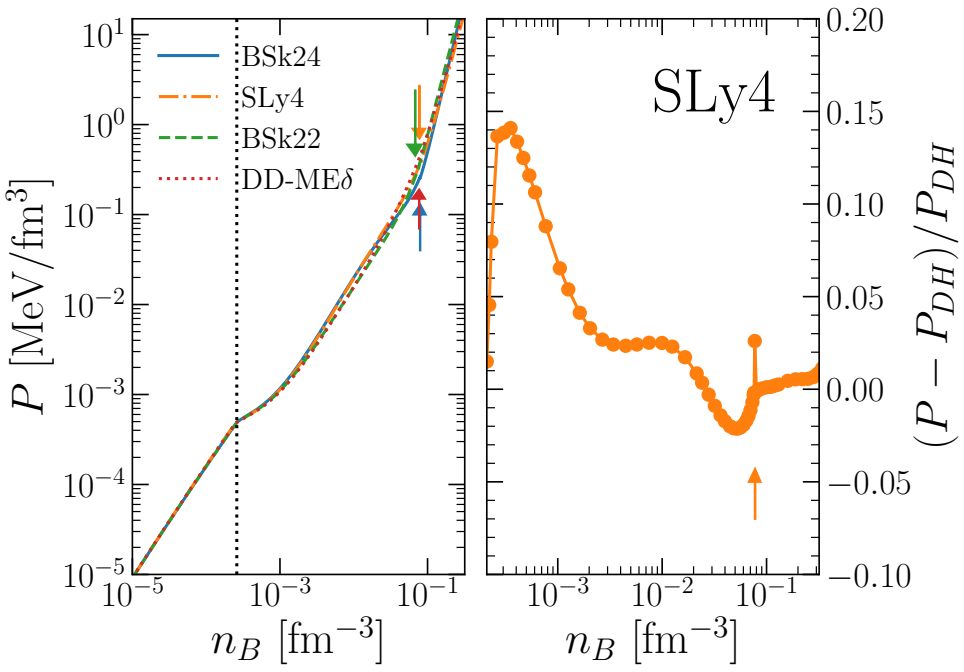

Figure 1.15: Left: Pressure as a function of baryon density in the different regions of a NS for BSk24, SLy4, BSk22, and DD-MEδ. Crust and core are described in a unified manner, with the metamodeling technique. The black dotted line marks the onset of the inner crust, and arrows indicate the CC transition density for the different models. Right: Relative difference $(P - P_{DH})/P_{DH}$ with DH unified EoS for SLy4 [DH01] as a function of n_B. The arrow indicates our estimation of the CC transition density for SLy4.

thickness and $\approx 4\%$ for the radius. The main justification for working with nonunified EoS is that the core is responsible of most of the NS mass, thus one could simply match any crust EoS, for instance that of BPS in the outer crust [BPS71] plus that of BBP in the inner crust [BBP71], with its core EoS based on a different nuclear interaction. This is indeed sufficient if one is interested in observables such as the maximum mass. However, it obviously leaves a large freedom in the matching procedure. In addition, this amounts to consider that the crust segment is not model dependent, while we have clearly seen in 1.2.3.3 that the crust EoS is sensitive to the nuclear model, and is in particular correlated with the symmetry energy. It is therefore preferable to describe the crust and core in a unified manner.

Several unified EoS for cold non-accreting NS have been proposed in the literature. For instance, the well-known DH EoS [DH01] is based on the Skyrme SLy4 effective interaction [Cha+98]. In the inner crust, the authors use a version of the CLDM to calculate the energy of finite nuclei, the bulk term of which is given by the SLy4 functional in the infinite NM limit, which is also used to describe the outside neutron gas, and at

high density to calculate the $npe\mu$ matter energetics in the core. Let us notice that the EoS of the outer-crust ground state is taken from [HP94] in this work.
More recently, a series of unified EoS based on modern BSk functionals [GCP13] has been proposed [Pea+18]. In this work, the ground state of the outer crust is determined by application of the microscopic HFB method [Sam+02], and the ground state of the inner crust is calculated within the ETFSI approximation [Ons+08]. Also, a set of unified EoS were built within a relativistic mean-field approach (RMF) in [For+16].

One obvious reason explaining why crust and core matter are not consistently treated using the same microscopic interaction is that it is less trivial to evaluate the ground state of the inner crust in comparison to the ground state of matter in the core. Indeed, one can evaluate the inner-crust ground state within different many-body approaches, either using the CLDM, the semiclassical ETFSI method, or full HF calculations. While the two last methods are expected to be more precise with respect to the CLD approximation as far as the composition is concerned, they can become computationally heavy if one wants to compute the EoS for many nuclear models. In addition, these more microscopic methods can only be extended to finite temperature in the SNA, whereas the CLD approximation allows distributions of clusters, that exist at $T > 0$, to be considered.
In view to provide a unified and thermodynamically consistent treatment of the crust and core of cold non-accreting NS, we propose to compute the EoS within the metamodeling approach that we have presented throughout this chapter. For a given nuclear model, in other words a given set of empirical parameters $\boldsymbol{P_\alpha}$, we proceed as follows. The EoS in the outer crust is evaluated by application of the BPS method presented in 1.1.2, using the present day knowledge on experimental masses [Hua+17] supplemented by state-of-the-art microscopic HFB theoretical mass tables [GCP13] up to the neutron-drip point. The EoS in the inner crust is then calculated by solving the system of four differential equations, Eqs. (1.84), (1.85), (1.86), and (1.87). The metamodeling technique, discussed in 1.2.1.1, is used to calculate the neutron gas energy. The concept of metamodeling of homogeneous NM is extended to finite nuclei in the CLD approximation in order to evaluate the cluster energy, the bulk term of which is calculated with the same empirical parameters as the neutron gas. Finally, from the CC transition point, discussed in 1.2.6, the core EoS is computed by solving the two chemical equilibrium equations Eqs. (1.106) and (1.107). Again, the empirical parameters are the same as those used in the inner crust. Within such an approach, one can compute the unified EoS for any nuclear model. In addition, this method is not expensive from the computational point of view, which will allow us to make comprehensive statistical evaluations of the model uncertainties in Chapter 2.

The left panel of Fig. 1.15 shows the resulting unified EoS for the four nuclear models considered in this chapter: BSk24, SLy4, BSk22, and DD-MEδ. The neutron-drip point is represented by the vertical dotted line, and arrows indicate the CC transition density for each model.
The relative difference between the DH EoS [DH01] and our EoS for SLy4 is represented as a function of the baryon density in the right panel of Fig. 1.15. It is seen that the overall difference is smaller than 10% in the inner crust. The slight disagreement at low density comes from the fact that the onset of the inner crust is marked at $n_{ND} = 2.0905 \times 10^{-4}$ fm^{-3} in the DH EoS (calculated in [HP94]), which is low in comparison

with our estimation of the neutron drip density, $n_{ND} = 2.503 \times 10^{-4}$ fm^{-3}. Let us notice that the parametrization of the surface tension in both studies is different, therefore it might explain the difference between the two EoS at higher densities in the inner crust, in addition to the slight error introduced by the metamodel. In the core, we can observe that the relative difference is smaller that 1%.

1.5 Conclusion

In this chapter, we have first evaluated the ground state of the outer crust, which is obtained by the application of the BPS method, using recent experimental masses [Hua+17; Wel+17] supplemented by state-of-the-art microscopic HFB theoretical mass tables. We have shown that the outer-crust composition and so the EoS are entirely determined by the present day knowledge on experimental masses up to $n_B \approx 3 \times 10^{-5}$ fm^{-3}. At higher densities, we have observed the persistence of $N = 82$ for each of the four mass models considered.

We have proposed a version of the CLDM based on the metamodeling technique [MHG18a; MHG18b]. We have seen that the metamodel offers the possibility to reproduce any functional of nuclear matter very precisely, with a unique functional form. The parametrization of surface tension was suggested from microscopic calculations in the free neutron regime [RPL83], and surface and curvature parameters are fitted to experimental masses. We have used the CLDM to calculate the ground state of the inner crust, which is obtained by minimizing the energy density of matter at constant baryon density under the condition of overall charge neutrality. We have therefore derived a system of four coupled differential equations, corresponding to chemical and mechanical equilibrium conditions, that we have solved numerically using Broyden's method. The ground-state composition of the inner crust for BSk24 empirical parameters was presented, and a very good agreement with more microscopic approaches was observed concerning the value of $Z \approx 40$. We have also seen that the proton fraction is continuously decreasing, as in the outer crust. The inner crust EoS was computed and a positive correlation with the empirical parameter E_{sym} was revealed. We have shown that magic numbers, that vanish within the CLD approach, can be recovered by adding perturbatively Strutinsky shell corrections on top of the CLD energy. In this way, a very good agreement with ETFSI calculations was observed for recent BSk functionals [Pea+18]. With the CLDM, we have explored the possible presence of nonspherical pasta phases in the bottom layers of the inner crust, finding the sequence spheres $\rightarrow$ cylinders $\rightarrow$ plates $\rightarrow$ tubes for each of the four model considered: BSk24, SLy4, BSk22, and DD-MEδ. We have shown that the transition point to homogeneous matter is very sensitive to the surface tension at extreme values of isospin, the behavior of which is governed by the isovector surface parameter p. Unfortunately, this parameter cannot be accessed from empirical nuclear physics data, which are limited to values around $I \lesssim 0.3$. We have seen that the CC transition density and pressure results of the literature for the dynamical spinodal [Duc+11] are globally nicely reproduced by our calculation from the crust with $p \approx 3$. We have also confirmed the correlation of the transition density n_t with the empirical parameter L_{sym} already observed in previous works.

We have derived the equilibrium equations characterizing the ground state of matter

in the core, which consists of $npe\mu$ matter up to $n_B \approx 2n_{sat}$. The strong correlation between the symmetry energy and the proton fraction was explained. We have found that muons appear in the vicinity of $n_B \approx 0.12$ fm^{-3} for each model. As in previous works [WFF88; DH01], we have extrapolated the npeμ model to higher densities, since the hyperon-hyperon and hyperon-nucleon interactions remain currently poorly constrained.

Finally, we have stressed that building unified EoS is essential to properly estimate crustal observables. In that sense we have proposed a metamodeling of the EoS of cold non-accreting NS, where the crust and core are treated in a uniform manner, that is with the same empirical parameters. Using the SLy4 empirical parameters, we have shown that the relative difference with the DH EoS is smaller than 10% in the inner crust and 1% in the core.

In Chapter 2, we will exploit the second advantage of the metamodeling technique, namely the fact that no artificial correlations are introduced a priori among the empirical parameters, to carry out complete statistical analyses that will allow us to settle the model dependence of the results.

Appendix A

Energy density of a relativistic electron gas

We give here the derivation of the energy density of a relativistic electron gas of density n_e at zero temperature.

From $\approx 10^{14}$ g/cm^3, electrons are essentially free. In this case, the energy density is given by

$$\varepsilon_e = \frac{c}{\pi^2}\int_{k=0}^{k_e} dk k^2 \sqrt{\hbar^2 k^2 + m_e^2 c^2}, \tag{A.1}$$

c being the speed of light, $\hbar$ the reduced Planck constant, and m_e the electron mass. The electron Fermi wave number k_e is related to the electron density via $k_e = (3\pi^2 n_e)^{1/3}$. Making a simple variable, $x = \hbar k/(m_e c)$, we can rewrite the energy density as

$$\varepsilon_e = \frac{m_e^4 c^5}{\pi^2 \hbar^3}\xi(x_r) \tag{A.2}$$

with $x_r = \hbar k_e/(m_e c)$ and

$$\xi = \int_{x=0}^{x_r} dx x^2 \sqrt{x^2+1}. \tag{A.3}$$

Integrating by parts, it follows

$$\begin{aligned}
\xi &= \left[\frac{x^3}{3}\sqrt{x^2+1}\right]_0^{x_r} - \int_0^{x_r} dx \frac{x^4}{3\sqrt{x^2+1}} \\
3\xi &= x_r^3\sqrt{x_r^2+1} - \int_0^{x_r} dx x^2 \left(\frac{x^2+1}{\sqrt{x^2+1}} - \frac{1}{\sqrt{x^2+1}}\right) \\
4\xi &= x_r^3\sqrt{x_r^2+1} + \int_0^{x_r} dx \frac{x^2}{\sqrt{x^2+1}}.
\end{aligned} \tag{A.4}$$

We have

$$\frac{d}{dx}\left(x\sqrt{x^2+1}\right) = \sqrt{x^2+1} + \frac{x^2}{\sqrt{x^2+1}}, \tag{A.5}$$

and

$$\frac{d}{dx}\left[\ln(x+\sqrt{x^2+1})\right] = \sqrt{x^2+1} - \frac{x^2}{\sqrt{x^2+1}}. \tag{A.6}$$

thus,

$$\frac{1}{2}\frac{d}{dx}\left[x\sqrt{x^2+1}-\ln\left(x+\sqrt{x^2+1}\right)\right]=\frac{x^2}{\sqrt{x^2+1}}. \tag{A.7}$$

Hence,

$$4\xi = x_r^3\sqrt{x_r^2+1}+\frac{1}{2}\left[x\sqrt{x^2+1}-\ln\left(x+\sqrt{x^2+1}\right)\right]_0^{x_r}, \tag{A.8}$$

which finally gives

$$\varepsilon_e(n_e)=\frac{m_e^4c^5}{8\pi^2\hbar^3}\left[x_r(2x_r^2+1)\gamma_r-\ln(x_r+\gamma_r)\right], \tag{A.9}$$

where we have introduced the parameter parameter $\gamma_r=\sqrt{x_r^2+1}$.

Appendix B

Neutron and proton chemical potentials in the metamodel

From the metamodeling of the nuclear matter energy, Eq. 1.37, we give here the complete expressions of the neutron and proton chemical potentials for a homogeneous system characterized by a neutron density n_n and proton density n_p at zero temperature. Let us introduce the variables $x = (n - n_{sat})/(3n_{sat})$ and $\delta = (n_n - n_p)/n$, $n = n_n + n_p$ being the total baryon density.

The neutron chemical potential, with the rest mass energy $m_n c^2$, is given by

$$\mu_{HM,n} = e_{HM}(n_n, n_p) + n\left(\frac{\partial e_{HM}}{\partial n_n}\right)_{n_p} + m_n c^2 \quad \text{(B.1)}$$

$$\mu_{HM,n} = e_{HM}(n, \delta) + \frac{1+3x}{3}\left(\frac{\partial e_{HM}}{\partial x}\right)_{\delta} + (1-\delta)\left(\frac{\partial e_{HM}}{\partial \delta}\right)_{x} + m_n c^2. \quad \text{(B.2)}$$

Equivalently, the proton chemical potential is given by

$$\mu_{HM,p} = e_{HM}(n, \delta) + \frac{1+3x}{3}\left(\frac{\partial e_{HM}}{\partial x}\right)_{\delta} - (1+\delta)\left(\frac{\partial e_{HM}}{\partial \delta}\right)_{x} + m_p c^2. \quad \text{(B.3)}$$

We first go through the derivative with respect to x, yielding

$$\begin{aligned}\left(\frac{\partial e_{HM}}{\partial x}\right)_{\delta} = & \frac{5}{1+3x} t_{HM}^{FG}(n, \delta) \\ & - \frac{3}{1+3x}\frac{1}{2} t_{sat}^{FG}(1+3x)^{2/3}\left[(1+\delta)^{5/3} + (1-\delta)^{5/3}\right] \\ & + \sum_{\alpha \geq 0}(v_\alpha^{is} + v_\alpha^{iv}\delta^2)\frac{1}{\alpha!}\left(\alpha x^{\alpha-1} u_\alpha(x) + x^\alpha \frac{du_\alpha}{dx}\right). \end{aligned} \quad \text{(B.4)}$$

Let us notice that is gives the expression for the total pressure,

$$P_{HM}(n, \delta) = n^2\left(\frac{\partial e_{HM}}{\partial n}\right)_{\delta} \quad \text{(B.5)}$$

$$= \frac{1}{3} n_{sat}(1+3x)^2\left(\frac{\partial e_{HM}}{\partial x}\right)_{\delta}. \quad \text{(B.6)}$$

We now turn to the derivative with respect to the asymmetry δ,

$$\begin{aligned}\left(\frac{\partial e_{HM}}{\partial \delta}\right)_x &= \frac{1}{2}t_{sat}^{FG}(1+3x)^{5/3}\left[(1+\delta)^{5/3}-(1-\delta)^{5/3}\right] \\ &+\frac{5}{6}t_{sat}^{FG}(1+3x)^{2/3}\left[(1+\delta)^{2/3}\frac{m}{m_n^*}-(1-\delta)^{2/3}\frac{m}{m_p^*}\right] \\ &+2\delta\sum_{\alpha\geq 0}v_\alpha^{iv}\frac{x^\alpha}{\alpha!}u_\alpha(x). \end{aligned} \tag{B.7}$$

Appendix C

Total pressure in the inner crust

Bibliography

[Abb+18] B. P. Abbott et al. "GW170817: Measurements of Neutron Star Radii and Equation of State". In: *Phys. Rev. Lett.* 121 (16 Oct. 2018), p. 161101. DOI: 10.1103/PhysRevLett.121.161101.

[Abb+19] B. P. Abbott et al. "Properties of the Binary Neutron Star Merger GW170817". In: *Phys. Rev. X* 9 (1 Jan. 2019), p. 011001. DOI: 10.1103/PhysRevX.9.011001.

[Ant+13] John Antoniadis et al. "A Massive Pulsar in a Compact Relativistic Binary". In: *Science* 340.6131 (2013). DOI: 10.1126/science.1233232. eprint: https://science.sciencemag.org/content/340/6131/1233232.full.pdf.

[Ant+19] Sofija Antić et al. "Quantifying the uncertainties on spinodal instability for stellar matter through meta-modeling". In: *Journal of Physics G: Nuclear and Particle Physics* 46.6 (May 2019), p. 065109. DOI: 10.1088/1361-6471/ab1a51.

[APR98] A. Akmal, V. R. Pandharipande, and D. G. Ravenhall. "Equation of state of nucleon matter and neutron star structure". In: *Phys. Rev. C* 58 (3 Sept. 1998), pp. 1804–1828. DOI: 10.1103/PhysRevC.58.1804.

[Aud+12] G. Audi et al. "The Ame2012 atomic mass evaluation". In: *Chinese Physics C* 36.12 (Dec. 2012), pp. 1287–1602. DOI: 10.1088/1674-1137/36/12/002.

[Ava+08] S. S. Avancini et al. "Warm and cold pasta phase in relativistic mean field theory". In: *Phys. Rev. C* 78 (1 July 2008), p. 015802. DOI: 10.1103/PhysRevC.78.015802.

[Ava+10] Sidney S. Avancini et al. "Warm "pasta" phase in the Thomas-Fermi approximation". In: *Phys. Rev. C* 82 (5 Nov. 2010), p. 055807. DOI: 10.1103/PhysRevC.82.055807.

[Bay+19] Gordon Baym et al. "New Neutron Star Equation of State with Quark-Hadron Crossover". In: *Astrophys. J.* 885.1, 42 (Nov. 2019), p. 42. DOI: 10.3847/1538-4357/ab441e. arXiv: 1903.08963 [astro-ph.HE].

[BBP71] Gordon Baym, Hans A. Bethe, and Christopher J Pethick. "Neutron star matter". In: *Nuclear Physics A* 175.2 (1971), pp. 225–271. DOI: https://doi.org/10.1016/0375-9474(71)90281-8.

[Bed+12] Bednarek, I. et al. "Hyperons in neutron-star cores and a $2M_{\odot}$ pulsar". In: *A&A* 543 (2012), A157. DOI: 10.1051/0004-6361/201118560.

[BPS71] Gordon Baym, Christopher Pethick, and Peter Sutherland. "The Ground state of matter at high densities: Equation of state and stellar models". In: *Astrophys. J.* 170 (1971), pp. 299–317. DOI: 10.1086/151216.

[Bro65] C. G. Broyden. "A Class of Methods for Solving Nonlinear Simultaneous Equations". In: *Mathematics of Computation* 19.92 (1965), pp. 577–593.

[BW39] Niels Bohr and John Archibald Wheeler. "The Mechanism of Nuclear Fission". In: *Phys. Rev.* 56 (5 Sept. 1939), pp. 426–450. DOI: 10.1103/PhysRev.56.426.

[Car+19] T. Carreau et al. "Crystallization of the inner crust of a neutron star and the influence of shell effects". In: (2019). arXiv: 1912.01265 [astro-ph.HE].

[Car17a] T. Carreau. https://github.com/thomascarreau/NSEoS. 2017.

[Car17b] T. Carreau. "Vers une description unifiée de la croûte et du coeur des étoiles à neutrons". MA thesis. Université de Caen-Normandie, 2017.

[CF16] N. Chamel and A. F. Fantina. "Binary and ternary ionic compounds in the outer crust of a cold nonaccreting neutron star". In: *Phys. Rev. C* 94 (6 Dec. 2016), p. 065802. DOI: 10.1103/PhysRevC.94.065802.

[CGM19] Carreau, Thomas, Gulminelli, Francesca, and Margueron, Jérôme. "Bayesian analysis of the crust-core transition with a compressible liquid-drop model". In: *Eur. Phys. J. A* 55.10 (2019), p. 188. DOI: 10.1140/epja/i2019-12884-1.

[Cha+07] N. Chamel et al. "Validity of the Wigner-Seitz approximation in neutron star crust". In: *Phys. Rev. C* 75 (5 May 2007), p. 055806. DOI: 10.1103/PhysRevC.75.055806.

[Cha+98] E. Chabanat et al. "A Skyrme parametrization from subnuclear to neutron star densities Part II. Nuclei far from stabilities". In: *Nuclear Physics A* 635.1 (1998), pp. 231–256. DOI: https://doi.org/10.1016/S0375-9474(98)00180-8.

[Cha06] Nicolas Chamel. "Effective mass of free neutrons in neutron star crust". In: *Nuclear Physics A* 773.3 (2006), pp. 263–278. DOI: https://doi.org/10.1016/j.nuclphysa.2006.04.010.

[DCG07] C. Ducoin, Ph. Chomaz, and F. Gulminelli. "Isospin-dependent clusterization of neutron-star matter". In: *Nuclear Physics A* 789.1 (2007), pp. 403–425. DOI: https://doi.org/10.1016/j.nuclphysa.2007.03.006.

[DH00] F Douchin and P Haensel. "Inner edge of neutron-star crust with SLy effective nucleon-nucleon interactions". In: *Physics Letters B* 485.1 (2000), pp. 107–114. DOI: https://doi.org/10.1016/S0370-2693(00)00672-9.

[DH01] Douchin, F. and Haensel, P. "A unified equation of state of dense matter and neutron star structure". In: *A&A* 380.1 (2001), pp. 151–167. DOI: 10.1051/0004-6361:20011402.

[DHM00] F Douchin, P Haensel, and J Meyer. "Nuclear surface and curvature properties for SLy Skyrme forces and nuclei in the inner neutron-star crust". In: *Nuclear Physics A* 665.3 (2000), pp. 419–446. DOI: https://doi.org/10.1016/S0375-9474(99)00397-8.

[DHS16] C. Drischler, K. Hebeler, and A. Schwenk. "Asymmetric nuclear matter based on chiral two- and three-nucleon interactions". In: *Phys. Rev. C* 93 (5 May 2016), p. 054314. DOI: 10.1103/PhysRevC.93.054314.

[DMC08] C. Ducoin, J. Margueron, and Ph. Chomaz. "Cluster formation in asymmetric nuclear matter: Semi-classical and quantal approaches". In: *Nuclear Physics A* 809.1 (2008), pp. 30–64. DOI: https://doi.org/10.1016/j.nuclphysa.2008.05.015.

[Duc+07] C. Ducoin et al. "Anomalous thermodynamics and phase transitions in neutron star matter". In: *Phys. Rev. C* 75 (6 June 2007), p. 065805. DOI: 10.1103/PhysRevC.75.065805.

[Duc+11] Camille Ducoin et al. "Core-crust transition in neutron stars: Predictivity of density developments". In: *Phys. Rev. C* 83 (4 Apr. 2011), p. 045810. DOI: 10.1103/PhysRevC.83.045810.

[Esp+11] C. M. Espinoza et al. "A study of 315 glitches in the rotation of 102 pulsars". In: *Monthly Notices of the Royal Astronomical Society* 414.2 (June 2011), pp. 1679–1704. DOI: 10.1111/j.1365-2966.2011.18503.x. eprint: https://academic.oup.com/mnras/article-pdf/414/2/1679/3015039/mnras0414-1679.pdf.

[FMT49] R. P. Feynman, N. Metropolis, and E. Teller. "Equations of State of Elements Based on the Generalized Fermi-Thomas Theory". In: *Phys. Rev.* 75 (10 May 1949), pp. 1561–1573. DOI: 10.1103/PhysRev.75.1561.

[For+15] M. Fortin et al. "Neutron stars with hyperon cores: stellar radii and equation of state near nuclear density". In: *Astron. Astrophys.* 576 (2015), A68. DOI: 10.1051/0004-6361/201424800. arXiv: 1408.3052 [astro-ph.SR].

[For+16] M. Fortin et al. "Neutron star radii and crusts: Uncertainties and unified equations of state". In: *Phys. Rev. C* 94 (3 Sept. 2016), p. 035804. DOI: 10.1103/PhysRevC.94.035804.

[Gan+14] Gandolfi, S. et al. "The equation of state of neutron matter, symmetry energy and neutron star structure". In: *Eur. Phys. J. A* 50.2 (2014), p. 10. DOI: 10.1140/epja/i2014-14010-5.

[GCP13] S. Goriely, N. Chamel, and J. M. Pearson. "Further explorations of Skyrme-Hartree-Fock-Bogoliubov mass formulas. XIII. The 2012 atomic mass evaluation and the symmetry coefficient". In: *Phys. Rev. C* 88 (2 Aug. 2013), p. 024308. DOI: 10.1103/PhysRevC.88.024308.

[Gon+17] C. Gonzalez-Boquera et al. "Higher-order symmetry energy and neutron star core-crust transition with Gogny forces". In: *Phys. Rev. C* 96 (6 Dec. 2017), p. 065806. DOI: 10.1103/PhysRevC.96.065806.

[Gor+05] S. Goriely et al. “Further explorations of Skyrme–Hartree–Fock–Bogoliubov mass formulas. IV: Neutron-matter constraint”. In: *Nuclear Physics A* 750.2 (2005), pp. 425–443. DOI: https://doi.org/10.1016/j.nuclphysa.2005.01.009.

[GPA12] Fabrizio Grill, Constan ça Providência, and Sidney S. Avancini. “Neutron star inner crust and symmetry energy”. In: *Phys. Rev. C* 85 (5 May 2012), p. 055808. DOI: 10.1103/PhysRevC.85.055808.

[Gra+17] Guilherme Grams et al. “Nuclear pasta phases within the quark-meson coupling model”. In: *Phys. Rev. C* 95 (5 May 2017), p. 055807. DOI: 10.1103/PhysRevC.95.055807.

[GSP07] S. Goriely, M. Samyn, and J. M. Pearson. “Further explorations of Skyrme-Hartree-Fock-Bogoliubov mass formulas. VII. Simultaneous fits to masses and fission barriers”. In: *Phys. Rev. C* 75 (6 June 2007), p. 064312. DOI: 10.1103/PhysRevC.75.064312.

[HP94] P. Haensel and B. Pichon. “Experimental nuclear masses and the ground state of cold dense matter”. In: *Astron. Astrophys.* 283 (1994), p. 313. arXiv: nucl-th/9310003 [nucl-th].

[HPY07] P. Haensel, A. Y. Potekhin, and D. G. Yakovlev. *Neutron stars 1: Equation of state and structure*. Vol. 326. 2007, pp.1–619. DOI: 10.1007/978-0-387-47301-7.

[Hua+17] W.J. Huang et al. “The AME2016 atomic mass evaluation (I). Evaluation of input data; and adjustment procedures”. In: *Chinese Physics C* 41.3 (Mar. 2017), p. 030002. DOI: 10.1088/1674-1137/41/3/030002.

[LPT03] D. Lunney, J. M. Pearson, and C. Thibault. “Recent trends in the determination of nuclear masses”. In: *Rev. Mod. Phys.* 75 (3 Aug. 2003), pp. 1021–1082. DOI: 10.1103/RevModPhys.75.1021.

[LRP93] C. P. Lorenz, D. G. Ravenhall, and C. J. Pethick. “Neutron star crusts”. In: *Phys. Rev. Lett.* 70 (4 Jan. 1993), pp. 379–382. DOI: 10.1103/PhysRevLett.70.379.

[LS08] Z. H. Li and H.-J. Schulze. “Neutron star structure with modern nucleonic three-body forces”. In: *Phys. Rev. C* 78 (2 Aug. 2008), p. 028801. DOI: 10.1103/PhysRevC.78.028801.

[LS91] James M. Lattimer and Douglas F. Swesty. “A generalized equation of state for hot, dense matter”. In: *Nuclear Physics A* 535.2 (Dec. 1991), pp. 331–376. DOI: 10.1016/0375-9474(91)90452-C.

[MHG18a] Jérôme Margueron, Rudiney Hoffmann Casali, and Francesca Gulminelli. “Equation of state for dense nucleonic matter from metamodeling. I. Foundational aspects”. In: *Phys. Rev. C* 97 (2 Feb. 2018), p. 025805. DOI: 10.1103/PhysRevC.97.025805.

[MHG18b] Jérôme Margueron, Rudiney Hoffmann Casali, and Francesca Gulminelli. "Equation of state for dense nucleonic matter from metamodeling. II. Predictions for neutron star properties". In: *Phys. Rev. C* 97 (2 Feb. 2018), p. 025806. DOI: 10.1103/PhysRevC.97.025806.

[MN88] P. Möller and J.R. Nix. "Nuclear masses from a unified macroscopic-microscopic model". In: *Atomic Data and Nuclear Data Tables* 39.2 (1988), pp. 213–223. DOI: https://doi.org/10.1016/0092-640X(88)90022-8.

[Mol+95] P. Moller et al. "Nuclear Ground-State Masses and Deformations". In: *Atomic Data and Nuclear Data Tables* 59.2 (1995), pp. 185–381. DOI: https://doi.org/10.1006/adnd.1995.1002.

[MS65] W. D. Myers and W. J. Swiatecki. "unpublished". In: *UCRL Report* 11980 (May 1965).

[MS66] William D. Myers and Wladyslaw J. Swiatecki. "Nuclear masses and deformations". In: *Nuclear Physics* 81.1 (1966), pp. 1–60. DOI: https://doi.org/10.1016/0029-5582(66)90639-0.

[MTC09] Toshiki Maruyama, Toshitaka Tatsumi, and Satoshi Chiba. "Equation of state of nuclear matter in the first order phase transition". In: *AIP Conference Proceedings* 1120.1 (2009), pp. 129–134. DOI: 10.1063/1.3141634. eprint: https://aip.scitation.org/doi/pdf/10.1063/1.3141634.

[NGL12] W. G. Newton, M. Gearheart, and Bao-An Li. "A SURVEY OF THE PARAMETER SPACE OF THE COMPRESSIBLE LIQUID DROP MODEL AS APPLIED TO THE NEUTRON STAR INNER CRUST". In: *The Astrophysical Journal Supplement Series* 204.1 (Dec. 2012), p. 9. DOI: 10.1088/0067-0049/204/1/9.

[NS09] W. G. Newton and J. R. Stone. "Modeling nuclear "pasta" and the transition to uniform nuclear matter with the 3D Skyrme-Hartree-Fock method at finite temperature: Core-collapse supernovae". In: *Phys. Rev. C* 79 (5 May 2009), p. 055801. DOI: 10.1103/PhysRevC.79.055801.

[NV73] J.W. Negele and D. Vautherin. "Neutron star matter at sub-nuclear densities". In: *Nuclear Physics A* 207.2 (1973), pp. 298–320. DOI: https://doi.org/10.1016/0375-9474(73)90349-7.

[Oer+17] M. Oertel et al. "Equations of state for supernovae and compact stars". In: *Rev. Mod. Phys.* 89 (1 Mar. 2017), p. 015007. DOI: 10.1103/RevModPhys.89.015007.

[Ons+08] M. Onsi et al. "Semi-classical equation of state and specific-heat expressions with proton shell corrections for the inner crust of a neutron star". In: *Phys. Rev. C* 77 (6 June 2008), p. 065805. DOI: 10.1103/PhysRevC.77.065805.

[Pap+13] P. Papakonstantinou et al. "Densities and energies of nuclei in dilute matter at zero temperature". In: *Phys. Rev. C* 88 (4 Oct. 2013), p. 045805. DOI: 10.1103/PhysRevC.88.045805.

[PCP20] J. M. Pearson, N. Chamel, and A. Y. Potekhin. "Unified equations of state for cold nonaccreting neutron stars with Brussels-Montreal functionals. II. Pasta phases in semiclassical approximation". In: *Phys. Rev. C* 101 (1 Jan. 2020), p. 015802. DOI: 10.1103/PhysRevC.101.015802.

[Pea+12] J. M. Pearson et al. "Inner crust of neutron stars with mass-fitted Skyrme functionals". In: *Phys. Rev. C* 85 (6 June 2012), p. 065803. DOI: 10.1103/PhysRevC.85.065803.

[Pea+18] J M Pearson et al. "Unified equations of state for cold non-accreting neutron stars with Brussels–Montreal functionals – I. Role of symmetry energy". In: *Monthly Notices of the Royal Astronomical Society* 481.3 (Sept. 2018), pp. 2994–3026. DOI: 10.1093/mnras/sty2413. eprint: https://academic.oup.com/mnras/article-pdf/481/3/2994/25817956/sty2413.pdf.

[Pea+19] J M Pearson et al. "Erratum: Unified equations of state for cold non-accreting neutron stars with Brussels-Montreal functionals. I. Role of symmetry energy". In: *Monthly Notices of the Royal Astronomical Society* 486.1 (Mar. 2019), pp. 768–768. DOI: 10.1093/mnras/stz800. eprint: https://academic.oup.com/mnras/article-pdf/486/1/768/28345283/stz800.pdf.

[Pea19] J. M. Pearson. Private communication. 2019.

[PR95] C. J. Pethick and D. G. Ravenhall. "Matter at large neutron excess and the physics of neutron-star crusts". In: *Ann. Rev. Nucl. Part. Sci.* 45 (1995), pp. 429–484. DOI: 10.1146/annurev.ns.45.120195.002241.

[PRL95] C.J. Pethick, D.G. Ravenhall, and C.P. Lorenz. "The inner boundary of a neutron-star crust". In: *Nuclear Physics A* 584.4 (1995), pp. 675–703. DOI: https://doi.org/10.1016/0375-9474(94)00506-I.

[Roc+11] X. Roca-Maza et al. "Relativistic mean-field interaction with density-dependent meson-nucleon vertices based on microscopical calculations". In: *Phys. Rev. C* 84 (5 Nov. 2011), p. 054309. DOI: 10.1103/PhysRevC.84.054309.

[RPL83] D.G. Ravenhall, C.J. Pethick, and J.M. Lattimer. "Nuclear interface energy at finite temperatures". In: *Nuclear Physics A* 407.3 (1983), pp. 571–591. DOI: https://doi.org/10.1016/0375-9474(83)90667-X.

[Sam+02] M. Samyn et al. "A Hartree–Fock–Bogoliubov mass formula". In: *Nuclear Physics A* 700.1 (2002), pp. 142–156. DOI: https://doi.org/10.1016/S0375-9474(01)01316-1.

[Vid+09] Isaac Vidaña et al. "Density dependence of the nuclear symmetry energy: A microscopic perspective". In: *Phys. Rev. C* 80 (4 Oct. 2009), p. 045806. DOI: 10.1103/PhysRevC.80.045806.

[Viñ+17] X. Viñas et al. "Crust-Core Transitions in Neutron Stars Revisited". In: *Bulg. J. Phys.* 44.S1 (2017), pp. 081–092.

[Wat+03] Gentaro Watanabe et al. "Structure of cold nuclear matter at subnuclear densities by quantum molecular dynamics". In: *Phys. Rev. C* 68 (3 Sept. 2003), p. 035806. DOI: 10.1103/PhysRevC.68.035806.

[Wel+17] A. Welker et al. “Binding Energy of ^{79}Cu: Probing the Structure of the Doubly Magic ^{78}Ni from Only One Proton Away”. In: *Phys. Rev. Lett.* 119 (19 Nov. 2017), p. 192502. DOI: 10.1103/PhysRevLett.119.192502.

[WFF88] R. B. Wiringa, V. Fiks, and A. Fabrocini. “Equation of state for dense nucleon matter”. In: *Phys. Rev. C* 38 (2 Aug. 1988), pp. 1010–1037. DOI: 10.1103/PhysRevC.38.1010.

[WM11] Gentaro Watanabe and Toshiki Maruyama. *Nuclear pasta in supernovae and neutron stars*. 2011. arXiv: 1109.3511 [nucl-th].

[WS33] E. Wigner and F. Seitz. “On the Constitution of Metallic Sodium”. In: *Phys. Rev.* 43 (10 May 1933), pp. 804–810. DOI: 10.1103/PhysRev.43.804.

[Yas+14] Nobutoshi Yasutake et al. “Finite-size effects at the hadron-quark transition and heavy hybrid stars”. In: *Phys. Rev. C* 89 (6 June 2014), p. 065803. DOI: 10.1103/PhysRevC.89.065803.

[YMT09] Nobutoshi Yasutake, Toshiki Maruyama, and Toshitaka Tatsumi. “Hot hadron-quark mixed phase including hyperons”. In: *Phys. Rev. D* 80 (12 Dec. 2009), p. 123009. DOI: 10.1103/PhysRevD.80.123009.

[YMT11] Nobutoshi Yasutake, Toshiki Maruyama, and Toshitaka Tatsumi. “Pasta Structures of Quark-Hadron Phase Transition in Proto-Neutron Stars”. In: *Journal of Physics: Conference Series* 312.4 (Sept. 2011), p. 042027. DOI: 10.1088/1742-6596/312/4/042027.

[ZH13] J. L. Zdunik and P. Haensel. “Maximum mass of neutron stars and strange neutron-star cores”. In: *Astron. Astrophys.* 551 (2013), A61. DOI: 10.1051/0004-6361/201220697. arXiv: 1211.1231 [astro-ph.SR].